Faculdade de Engenharia da Universidade do Porto

Viscous flow in enhanced geothermal systems under non-isothermal conditions

---

Author
Rui Pedro Sant' Ovaia da Silva Oliveira

Supervisor
Célio Bruno Pinto Fernandes (FEUP)

Master in Mechanical Engineering
January 2024

Abstract

This thesis explores the dynamics of viscous flow in evolving porous media under non-isothermal conditions, with a focus on its implications for enhanced geothermal systems (EGS). The study delves into the principles of geothermal energy and the fluids commonly used in geothermal applications. Recognizing the challenge of short-circuiting (fluid forming preferential flow paths) in rock formations and its impact on system efficiency when using traditional Newtonian fluids, the research investigates the potential of thermo-responsive fluids to mitigate these inefficiencies.

The primary objective involves a comparative analysis between a thermo-responsive fluid, specifically the thermo-thickening polymer SDKP, and water within the context of a Downhole Heat Exchanger (DHE), a specific geometry for EGS. Using computational fluid dynamics (CFD) simulations, this study employs the finite-volume method available in the OpenFOAM framework to obtain numerical solutions for the EGS exploration.

The methodology encompasses the selection of SDKP as the thermo-thickening polymer, followed by a comprehensive rheological characterization using the Herschell-Bulckley model with a Cross-WLF relation for the viscosity temperature dependence. The DHE geometry is then designed accordingly to an in-site location, and the mesh was generated with the cfMesh application.

Key findings reveal that, despite the thermo-thickening potential of the polymer, water remains the preferred choice for the studied DHE geometry. However, the thermo-thickening effect proved advantageous, enabling the polymer fluid to attain a higher temperature compared to simulations conducted without considering this factor.

Keywords: Enhanced Geothermal System; Thermo-Thickening Fluids; Computational Fluid Dynamics; Finite Volume Method; OpenFOAM.

Resumo

O tema desta tese é estudar escoamentos viscosos em meios porosos sob condições não isotérmicas, com foco nas suas implicações para os Sistemas Geotérmicos Aprimorados (SGA). O estudo aprofunda-se nos princípios da energia geotérmica e nos fluidos mais comuns a ser empregues em aplicações geotérmicas. Reconhecendo o desafio do "short-circuiting" (formação de caminhos preferenciais para o escoamento do fluido) em formações rochosas e o seu impacto na eficiência do sistema ao usar fluidos Newtonianos tradicionais (como a água), esta pesquisa investiga o potencial de fluidos termo-responsivos para mitigar essas ineficiências.

O principal objetivo envolve uma análise comparativa entre um fluido termo-responsivo, especificamente o polímero que aumenta a viscosidede com a temperatura SDKP, e a água no contexto de um Pemutador de Calor em Poço ("Downhole Heat Exchanger" - DHE), um tipo de geometria para SGA. Utilizando simulações numéricas de mecânica de fluidos computacional, neste estudo o método dos volumes finitos implementado no código OpenFOAM é usado para obter soluções numéricas para exploração de SGA.

A metodologia abrange a seleção do SDKP como polímero termo-espessante, seguido por uma caracterização reológica usando o modelo Herschell-Bulckley com a relação Cross-WLF para determinar a viscosidade em função da temperatura. Uma geometria de DHE é então projetada de acordo com uma localização *in-site*, e a geração da malha é feita pela aplicação *cfMesh*.

As principais descobertas revelam que, apesar do potencial do polímero termo-espessante, a água permanece a escolha preferida para a geometria estudada do DHE. No entanto, o efeito termo-espessante mostrou-se vantajoso, permitindo que o fluido polimérico atingisse uma temperatura mais elevada em comparação com simulações realizadas sem considerar esse fator.

Palavras-chave: Sistema Geotérmico Aprimorado; Fluidos Termoespessantes; Mecânica de Fluidos Computacional; Método dos Volumes Finitos; OpenFOAM.

Acknowledgements

I am sincerely grateful to all who contributed to the successful completion of this thesis, marking a challenging, but enriching journey. My heartfelt appreciation goes to my thesis supervisor, Célio Fernandes, for his unwavering guidance, expertise, and steadfast support from the inception of the project to its completion. Professor Célio not only proposed the theme, but saw it through to the end, providing invaluable assistance during the numerical simulations using OpenFOAM and the RheoTool library. His years of experience and his feedback and commitment significantly shaped the direction of this work.

I extend my gratitude to my friends, girlfriend, and family for their ongoing encouragement and support, standing by me through the highs and lows of this academic pursuit. Their unwavering belief has been a constant source of strength.

This thesis is a culmination of the collective efforts and support of all those mentioned above, and I am truly grateful for the collaborative spirit that has enriched this academic journey.

Contents

Nomenclature

Acronyms

AM	Acrylamide
AMPS	2-acrylamido-2-methylpropanesulfonic acid
CFD	Computational Fluid Dynamics
CPG	CO_2-Plume Geotherma
CS	Chisotan
DHE	Downhole Heat Exchanger
DVB	Divinylbenzene
EGS	Enhanced geothermal system
FDM	Finite differences method
FEM	Finite element method
FVM	Finite volume method
GNF	Generalized Newtonian Fluid
GPAM	Chitosan-g-polyacrylamide
HDR	Hot dry rock
LANL	Los Alamos National Laboratory
LCST	Lower critical solution temperature
LSFBF	Low-solid freshwater base fluid
NaAMPS	Sodium 2-acrylamido-2-methylpropanesulfonate
NSFBF	Non-solid freshwater base fluid
NCVL	N-vinylcaprolactam
ORC	Organic Rankine Cycle
PNIPAm	Poly(N-isopropylacrylamide
PNVCL	Poly(N-vinylcaprolactam)

SHM	Surfactant-character hydrophobic monomer
SIMPLE	Semi-Implicit Method for Pressure-Linked Equations
SIMPLEC	Semi-Implicit Method for Pressure-Linked Equations-Consistent
SCOO$_2$	Supercritical carbon dioxide
WLF	Williams-Landel-Ferry

Latin Symbols

$\boldsymbol{c_P}$	Specific heat capacity [J/ kg °C]
$\boldsymbol{Co}$	Courant number
$\boldsymbol{f}$	External forces [N]
$\boldsymbol{g}$	Gravitational acceleration vector [m/s^2]
$\boldsymbol{h}$	Height [m]
$\boldsymbol{k}$	Thermal conductivity [W/m °C]
$\boldsymbol{m}$	Mass [kg]
$\boldsymbol{n}$	Flow behavior index
$\boldsymbol{p}$	Pressure [Pa]
$\boldsymbol{p_{rgh}}$	Static pressure subtracted from the hydrostatic pressure [Pa]
$\boldsymbol{R_T}$	Heat transferred by radiation [J]
$\boldsymbol{S_T}$	Volumetric source of energy [J]
$\boldsymbol{t}$	Time [s]
$\boldsymbol{u}$	Velocity vector [m/s]
$\boldsymbol{U}$	Velocity magnitude [m/s]
$\boldsymbol{u_z}$	Velocity magnitude in the z direction [m/s]
$\boldsymbol{x}$	x component of position vector [m]
$\boldsymbol{y}$	y component of position vector [m]
$\boldsymbol{z}$	z component of position vector [m]

Greek Symbols

$\boldsymbol{\beta}$	Thermal expansion coefficient [$^\circ C^{-1}$]
$\boldsymbol{\dot{\gamma}}$	Shear-rate [s^{-1}]
$\boldsymbol{\Delta}$	Variation
$\boldsymbol{\eta}$	Viscosity of the polymer [$kg \cdot m \cdot s$]
$\boldsymbol{\mu}$	Newtonian viscosity [$kg \cdot m \cdot s$]
$\boldsymbol{\rho}$	Density [kg/m^3]
$\boldsymbol{\tau}$	Viscous stress [Pa]
$\boldsymbol{\tau_0}$	Yield stress [Pa]

List of Figures

List of Tables

Chapter 1

Introduction

1.1 Geothermic process

Geothermal energy is the energy stored within the Earth's core. While this immense heat resource is abundant in the Earth's crust and even deeper layers, its distribution is uneven, rarely concentrated, and often lies at too great a depth for utilization. With the growing search for cleaner energy sources, geothermal energy has emerged as a promising technology, especially compared to other renewable energy sources such as wind or solar because of its low intermittence.

This energy is mainly created from two different sources. The first contribution comes from the primordial energy remaining from the creation of the earth, and thus only decreases with time as it is not being created anymore. The other source is the radiogenic heat, that is energy released from the decay of radioactive elements such as potassium-40 (^{40}K), thorium-232 (^{232}Th), uranium-235 (^{235}U) and uranium-238 (^{238}U) [1]. It is currently estimated that half of the energy on Earth comes from each process [2].

Notice that the geothermal heat rises from the Earth's interior to the surface, dissipating along the way. Its presence becomes evident through the increase in the temperature in the rocks as we dive deeper into the Earth, creating a geothermal gradient, which averages around 30 °C per kilometer of depth [3]. In theory, it is possible to access the earth's heat almost everywhere, and it is particularly easy to tap this energy in areas where there is existing volcanic activity. These specific regions within the Earth's crust can be reached through drilling, and in these areas the temperature gradient significantly exceeds the typical average [4]. In addition, in these locations, geothermal resources could be presented in different ways. Conventional technologies work in what are called hydrothermal systems. In these systems, the heat is extracted from steam or, more commonly, hot water. The main problem with these reservoirs is their limited exploitable useful life. They can only be used until most of the fluid contained in them has been extracted. In this way, these geothermal reserves are similar to oil reserves [5]. On top of that, these locations are also the exception, rather than the rule. The vast majority of the accessible geothermal resources in the world are found in hot but dry rock. These systems are called hot dry rock (HDR) systems[6]. This led scientists to develop alternative technologies.

HDR reservoirs, first introduced in the 1970s, are man-made rock reservoirs created by fracturing rocks. This allows any suitable location of hot dry rock in the Earth's crust, at a reachable depth, to serve as an artificial reservoir. To harness this energy, a pair of wells is drilled into the rock, one serving as an injection well and the other as a production well. The water is circulated through the injection well and through the HDR reservoir, which acts as a heat exchanger. The fluid then returns to the surface through the production well, transferring heat. Geothermal systems that use HDR reservoirs are called Enhanced Geothermal Systems (EGS). This concept is described as extracting heat from 'tight' rock that has not fractured naturally, where permeability is generally low. To improve the permeability in hot rock, the number of natural pathways created by fractures in the rock is increased using a hydraulic overpressure process.

The first time HDR was researched was in the Los Alamos National Laboratory (LANL) in the USA, and its first implementation was Fenton Hill, which worked from 1974 to 1979 and by 1986, the thermal capacity of the system was around 10 MW. The success of this project confirmed the great potential of EGS. Several other EGSs have been implemented around the world. The location of some of the biggest ones can be seen in Figure 1.1. In the EU, EGSs began being developed at the Soultz plant in France and the Landau plant in Germany. The Soultz plant was the first commercial-scale EGS power plant to be operated in the world. It started from the European Geothermal Hot Dry Rock Project and its conception began in 1987 along with its operation in 2009 [7]. It was constructed in Soultz due to the fact that this location had a very high geothermal gradient of 11 °C per 100 m [8]. This leads to a reservoir temperature of more than 180 °C, which in turn leads to a production of 1.7 MW using an Organic Rankine Cycle (ORC).

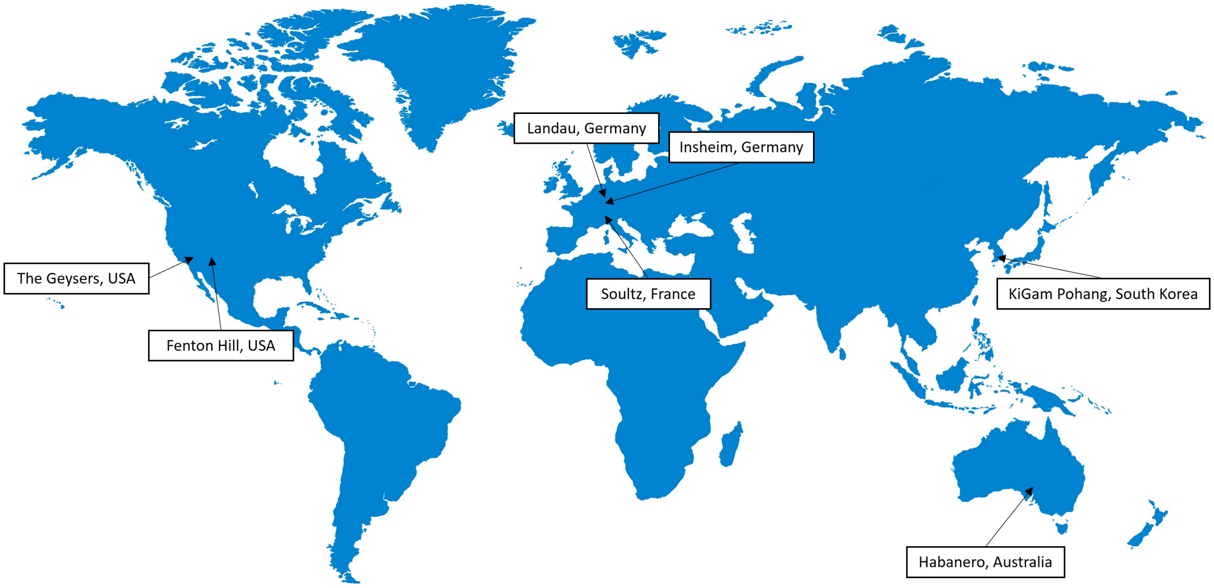

Figure 1.1: Illustration of global EGS sites distribution. Adapted from Lu [9]. World map image designed by rawpixel.com / Freepik.

In order to obtain good performance of the EGS, the choice of the injected fluid is of the most importance because of a technique called hydraulic stimulation. Hydraulic stimulation is used to create an underground heat exchanger that offers little resistance to fluid passage through the hot rock. Then, the density of the fluid can be adjusted so that the passage of it into the fractures improves the efficiency. Therefore, the use of dense fluids improves circulation pathways, the mass flow rate, and the heat extraction ratio [5].

1.2 Literature review of Enhanced Geothermal Systems' fluids

The first EGS created (Fenton Hill) used water as the fluid injected into the reservoir. This seems like a reasonable choice; In conventional EGS, water has been the most widely used fluid due to its high heat capacity and extensive resources [10]. However, water also has problems, with one major one being the water loss experienced in the cycle. In the Fenton Hill power plant, water losses were recorded up to 12% of the injected mass flow rate [6].

In 2000, carbon dioxide (CO_2) was proposed to replace water in EGS. This is because CO_2 under conditions of temperature and pressure above 30.98 °C and 7.39 MPa is in a supercritical state where its density changes slightly to lower than that of liquid water, but the viscosity and diffusivity are close to those of a gas. An advantage of using supercritical CO_2 ($SCCO_2$) is the fact that it exhibits a change in density with temperature (960 kg/m^3 for cold $SCCO_2$ and 390 kg/m^3 for hot $SCCO_2$) which creates a buoyant force and therefore requires less pumping power. Although $SCCO_2$ showed some disadvantages compared to water (for example, having a lower mass heat capacity and lower density), due to the advantages it has, the power production from an SCCO2 system is almost equal to that of a water-based system [11]. The last reason CO_2 showed promise compared to water, and perhaps the biggest one, is that the flow rate losses were seen as positive rather than negative. CO_2 created from combustion in fossil fuel power plants can be used as fracturing fluid and heat transport fluid in EGS. This CO_2 would then be continuously sequestered by diffusion into the rock mass surrounding the HDR reservoir. This technology to combine geothermal energy with geological CO_2 sequestration is called CO_2-Plume Geothermal (CPG) and provides a great way to create green energy, especially from a non-green process such as fossil fuel combustion.

While CO_2 showed great promise compared to water, it is still a Newtonian fluid and will still face the problem these fluids face in this type of operation. This problem is called short circuiting, which is a consequence of the positive feedback loop created by thermo-hydromechanical interaction within the rock mass [12]. In other words, Newtonian fluid injected into the rock will create preferential flow paths that will reduce the overall efficiency of the system. One way to solve this would be to use a non-Newtonian fluid that could change its viscosity with temperature and dynamically regularize the flow field in a fracture system that evolves over time. Fluids that can respond to external stimuli, such as temperature, are called stimuli-responsive.

Stimuli-responsive polymers are a class of polymers that respond to different types of stimuli, such as pH, temperature, and electric/magnetic fields [13]. Of these, one of the most popular is the thermoresponsive polymers. These show discontinuous changes in their physical properties with changes in temperature. Polymers showing a decrease in solubility with increasing temperature are known to exhibit a phenomenon called lower critical solution temperature (LCST) which is the lowest temperature at which temperature-induced demixing occurs. That is, below the LCST the polymer chains and solvent molecules are in one homogeneous mixed phase and above the LCST, phase separation occurs via an entropically driven process [14]. Some of the most popular polymers that exhibit LCST are Poly(N-isopropylacrylamide) (PNIPAm) and Poly(N-vinylcaprolactam) (PNVCL). These polymers show a similar LCST behavior in water between 30 and 32 °C [15]. They can also be combined with other materials to create more complex thermo-responsive polymers.

Thermoresponsive polymers have a wide range of potential applications in petroleum engineering and geothermal energy. In these industries, associative polymers are often used as rheology additives in drilling fluids to change the properties of the fluid under specific drilling conditions. This is because, for drilling operations in areas with high temperatures and high salinities, conventional polymers become limited because they show shear thinning behavior at high temperatures, which induces a relatively poor sweep efficiency of the aqueous displacement medium [16]. Therefore, thermo-thickening fluids are a solution to this problem. Thermo-thickening polymers are copolymers composed of a water-soluble main polymer and a low fraction of relatively small segments of a polymer with LCST in water [17]. Over the past decade, several advancements have been made in this area with the synthesis of several thermo-thickening polymers. Some of the most promising are presented below.

1.2.1 Sodium 2-acrylamido-2-methylpropane sulfonate with N - vinylcaprolactam and cross-linking divinyl benzene (SDKP)

In 2016, Xie et al. [18] developed the SDKP polymer. This polymer resembles the N-vinylcaprolactam (NVCL) monomer and showed great thermal stability in water-based fluids up to 230 °C. This fluid was synthesized using sodium 2-acrylamido-2-methylpropanesulfonate (NaAMPS), Nvinylcaprolactam (NVCL) divinylbenzene (DVB) by the micellar copolymerization technique. NVCL was used instead of NIPAm, the other very popular polymer that exhibited LCST, because in previous experiments Xie et al. [19] found that NIPAm tended to hydrolyze under high temperature and high salinity conditions after long-term interaction, resulting in an abrupt decrease in the viscosities of polymer solutions. In 2017, the same researchers studied the thermo-associating behavior of this polymer [20]. To do this, two water-based drilling fluids were developed: non-solid freshwater base fluid (NSFBF) and low-solid freshwater base fluid (LSFBF). NSFBF was created by adding SDKP to distilled water, while LSFBF also had the addition of a bentonite base fluid. In this fluids, the viscosity increased with the increase in temperature until around 80-120°C (depending on the composition of the fluid). At these temperatures, the viscosity was approximately four times that of the viscosity at room temperature.

1.2.2 Chitosan-g-polyacrylamide (GPAM)

GPAM is a polymer that was first developed in 2018 and also showed thermo-thickening behavior [21]. For the synthesis of this polymer, chitosan (CS) was chosen among other thermo-thickening materials, because it is the second most abundant polysaccharide after cellulose in nature, in addition to having good biocompatibility. The polymer showed an increase in viscosity with temperature to around 80 °C. However, this viscosity was very prone to being influenced by the heating history. This incomplete reversibility could be due to thermodynamic processes with intrinsic hysteresis.

1.2.3 Hydrophobic thermo-thickening polymer (HTP)

HTP was first synthesized in 2019 and its creators had the goal of creating a water-soluble polymer that had a continuous thermo-thickening ability in a wide temperature range [22]. This is because an ideal cement slurry for the exploration of oil and gas reserves should have a high viscosity for a large temperature range. This polymer was created using acrylamide (AM), 2-acrylamido-2-methylpropanesulfonic acid (AMPS) and a surfactant-character hydrophobic monomer (SHM). It showed thermo-thickening behavior in a large temperature range (48–148 °C) as intended and was especially successful when compared to a simpler polymer like a PNIPAm-based copolymer.

1.3 Objectives and goals

The motivation behind this research lies in exploring approaches to enhance the efficiency of EGS through the introduction of thermo-thickening fluids in opposition to water. To achieve this, numerical simulations were conducted using OpenFOAM software to model fluid flow within an EGS.

The objective of these simulations was to predict the flow fields, such as pressure, velocity and temperature, obtained for an EGS when imposing different temperature gradients and when using fluids with distinct rheological properties. To assess the viability of thermo-thickening fluids, a comparative analysis against water, the conventional geothermal working fluid should also be conducted with the aim of revealing any advantages or disadvantages associated with the use of thermo-thickening fluids in EGS, especially in simpler EGS like those with single-well configurations.

In addition to these goals, this research aims to speculate on what could be some advancements done in this area based on the results achieved by considering potential advancements, challenges, and innovations. By achieving these objectives, this thesis aims to provide insights into the use of thermo-thickening fluids in geothermal applications.

1.4 Thesis Outline

This work is divided into several sections that are outlined as follows.

- Methodology section

  The methodology employed in this study begins with an understanding of fluid behavior, differentiating between Newtonian and non-Newtonian fluids. The Herschel-Bulkley model was employed to provide a constitutive equation for the non-Newtonian fluids used on this work. A rheological characterization of these fluids was undertaken to delineate their essential properties and the time-temperature superposition principle was applied to characterize the temperature dependence of the material. In addition, the governing equations describing this non-isothermal fluid flow will be presented, as well as how they were discretized using the finite-volume method available in the OpenFOAM software.

- Case study section

  The case study section details the geometry employed in the simulations and outlining its relevance to EGS. It also explains how the mesh was created and what boundary conditions were employed. Additionally, the numerical parameters governing the simulation setup are introduced, explaining how they influence the accuracy and efficiency of the results obtained.

- Results and discussion

  The conclusion of the project lies in the presentation and discussion of the simulation results. This section provides a comprehensive analysis of the outcomes, elucidating the implications of using thermo-thickening fluids compared to conventional water-based systems in the context of EGS.

Chapter 2

Methodology

2.1 Rheological characterization

Within this project, a primary goal was to compare the efficacy of non-Newtonian thermo-thickening fluids in comparison to their Newtonian counterparts for EGS applications. To achieve this goal, water was selected as the Newtonian fluid, and SDKP was chosen as the thermo-thickening fluid due to its commendable thermo-thickening properties as discussed in Section 1. This study will then involve the comparison of three fluids: water, LSFBF, and NSFBF. The characterization of these fluids is presented in the following.

2.1.1 Newtonian fluids

Water is a Newtonian fluid and what this means is that at constant temperature and pressure, in simple shear, the shear rate ($\dot{\gamma}$) and the shear stress (τ) are proportional and thus the equation for the shear stress is:

$$\tau = \mu \cdot \dot{\gamma} \tag{2.1}$$

Here μ is the constant of proportionality and is called Newtonian viscosity. For almost all Newtonian fluids, an increase in temperature results in a decrease in viscosity. However, the viscosity of water was considered constant because the viscosity change with temperature is small for the temperature range considered in this work. This value was considered equal to $\mu_{\text{water}} = 0.001$ kg m^{-1} s^{-1}. The curve of shear stress versus shear rate for water, as well as for air as a comparison ($\mu_{air} = 10^{-5}$ kg m^{-1} s^{-1}), can be seen in Figure 2.1.

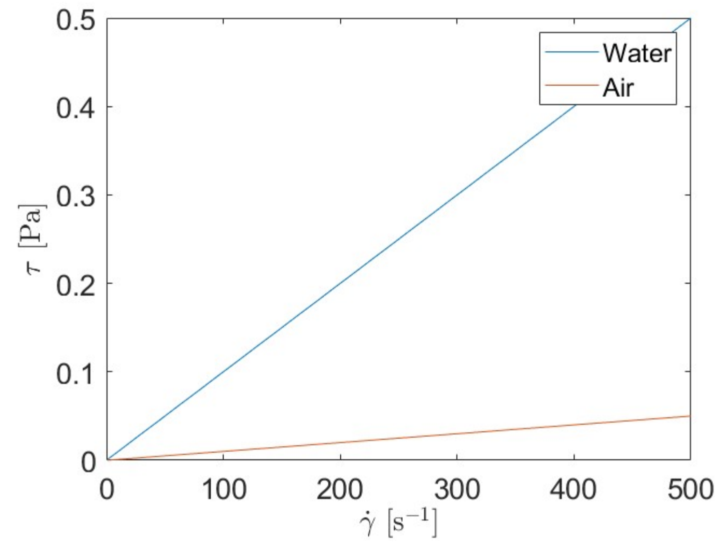

Figure 2.1: Shear stress vs. shear rate curve for water and air Newtonian fluids.

2.1.2 Non-Newtonian fluids

Although simpler fluids, such as water, air, or honey, exhibit Newtonian characteristics, the vast majority of known fluids present non-Newtonian behavior. In essence, a non-Newtonian fluid is characterized by a shear stress vs. shear rate curve that is not linear or does not intersect the origin [23]. These fluids can be categorized into various groups, each exhibiting distinct levels of complexity in their behavior. The simpler of these are the generalized Newtonian fluids (GNF).

Generalized Newtonian fluids are characterized by the fact that shear at any point within the fluid is solely determined by the shear stress value at that specific point and instant. They are also called purely viscous fluids or time-independent fluids. This is in contrast to more complex fluids, whose properties also rely on the kinematic history of the fluid, rendering them time-dependent. The typical equation that describes a GNF is as follows:

$$\tau = \eta(\dot{\gamma}) \cdot \dot{\gamma}, \tag{2.2}$$

where η is the apparent viscosity. The equation that describes this viscosity is called the fluid constitutive equation. Various models describe distinct behaviors within GNF, leading to different constitutive equations. These models can be categorized into:

- Shear-thinning or shear-thickening - depending on whether the viscosity decreases or increases, respectively, with an increase in the shear rate.
- Presenting or not presenting a yield stress (τ_0) - a yield stress signifies the stress level that must be attained before the fluid initiates flow. In the shear stress vs. shear rate curve, the presence of a yield stress is identifiable as the curve not intersecting the origin. Fluids that show yield stress are called viscoplastics.

Among the viscoplastic models, the Herschel-Bulkley fluid model is noteworthy [24]. This model characterizes a fluid with a non-linear shear rate curve coupled with the presence of a yield stress. Its equation is as follows.

$$\begin{cases} \tau = \tau_0 + m \cdot \dot{\gamma}^n & ,\text{for } \tau > \tau_0 \\ \dot{\gamma} = 0 & ,\text{for } \tau < \tau_0, \end{cases} \tag{2.3}$$

where m is the consistency index, n is the flow behavior index and τ_0 is the yield stress mentioned previously. If $n < 1$, then the fluid is shear-thinning: viscosity reduces with increasing shear rate. As the value of n reduces, the degree of shear thinning increases. For shear-thickening fluids (viscosity increases with increasing shear rate), $n > 1$. These constants are then adjusted according to the fluid.

Xie and Liu [20] studied the properties of SDKP and found that this polymer in the NSFBF and LSFBF formulations showed a behavior similar to that of a Herschel-Bulkley fluid. The constants m, τ_0 and n were then calculated for five different temperatures (30, 60, 90, 120 and 150 °C). The resulting values are presented in Table 2.1. As the value of n consistently remains below 1 in all cases, it indicates that both fluids exhibit shear-thinning behavior.

Table 2.1: Values for the Herschel-Bulkley constants at different temperatures. Adapted from Xie and Liu [20].

	T [°C]	τ_0 [Pa]	m [kg/m s^2]	n [kg/m s]
NSFBF	30	1.884	1.300	0.460
	60	1.762	1.594	0.462
	90	1.539	1.902	0.442
	120	1.234	1.521	0.438
	150	1.722	1.438	0.424
LSFBF	30	2.073	1.851	0.453
	60	1.837	2.111	0.426
	90	1.407	2.239	0.437
	120	1.217	2.241	0.405
	150	1.261	2.184	0.390

The equation for the viscosity in the Herschel-Bulkley model can be obtained by combining Equations (2.2) and (2.3), resulting in:

$$\eta(\dot{\gamma}) = \frac{\tau_0}{\dot{\gamma}} + m\ \dot{\gamma}^{n-1}. \tag{2.4}$$

Plotting the viscosity against the shear rate for these two SDKP fluids (see Figure 2.2), we can clearly see that the viscosity decreases with the increase in shear rate (shear-thinning) as well as increasing with the increase of temperature (thermo-thickening) up until around 90 °C and decreases after that.

The time-temperature superposition principle was used to obtain a single viscosity curve, which is dependent not only on the shear rate but also on the temperature. This is

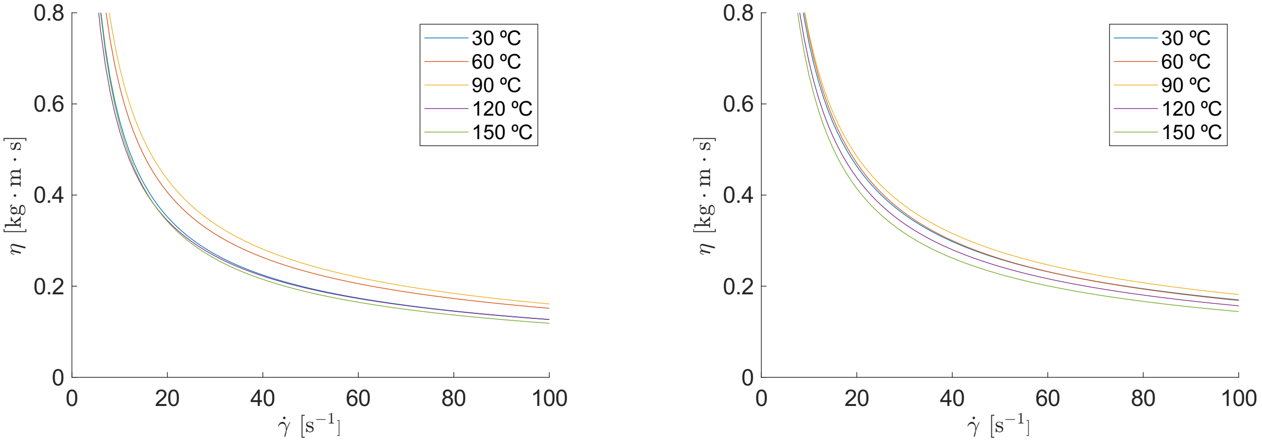

(a) NSFBF **(b)** LSFBF

Figure 2.2: Change in viscosity for the two SDKP fluids with the increase in temperature and shear rate.

achieved by multiplying the viscosity at a reference temperature (T_{ref}) by a function $f(T)$:

$$\eta(\dot{\gamma},T)=f(T)\left[\eta(\dot{\gamma})\right]_{T_{\mathrm{ref}}}. \tag{2.5}$$

Thus, we can modify Equation (2.4) to obtain:

$$\eta(\dot{\gamma},T)=f(T)\left(\frac{[\tau_0]_{T_{\mathrm{ref}}}}{\dot{\gamma}}+[m]_{T_{\mathrm{ref}}}\ \dot{\gamma}^{[n]_{T_{\mathrm{ref}}}-1}\right). \tag{2.6}$$

For both NSFBF and LSFBF, the reference temperature chosen was 90 °C. Subsequently, in order to obtain the expression for the function $f(T)$, Equation (2.6) can be modified to give:

$$f(T)=\frac{\tau_0(T)+m(T)\ \dot{\gamma}^{n(T)}}{[\tau_0]_{T=90^\circ C}+[m]_{T=90^\circ C}\ \dot{\gamma}^{[n]_{T=90^\circ C}}}. \tag{2.7}$$

Fluids were only studied for temperatures lower than 90 °C to obtain the thermo-thickening behavior throughout the simulation. Therefore, the Herschel-Bulkley constants for temperatures of 120 °C and 150 °C were ignored. Then, for the first three temperatures specified in Table 2.1 and for each $\dot{\gamma}$ value, a corresponding value for f can be derived. Since the variations of f are minimal for the various shear rates, an average was computed. The values obtained are presented in Table 2.2. To derive the function f, the only requirement is to select the type of a curve for fitting the experimental data. There are several functions available to scale the viscosity with the temperature, with one of the most popular being the Williams-Landel-Ferry (WLF) equation [25] which can be written as:

Table 2.2: Values of function $f(T)$ for several temperatures and each fluid.

	T [°C]		
	30	60	90
NSFBF	0.799	0.933	1
LSFBF	0.949	0.954	1

$$f(T) = 10^{-\frac{c_1\left(T - T_{ref}\right)}{c_2 + \left(T - T_{ref}\right)}}, \tag{2.8}$$

where c_1 and c_2 are constants that can be found by employing a fitting procedure. In order to obtain the constants that would best fit the values of Table 2.2, the MATLAB software with the Curve Fitting Toolbox were used. The resulting values as well as the regression coefficient R^2 for each of the fits are presented in Table 2.3. In addition to that, the graphs showing the curve fitting are presented in Figure 2.3.

Table 2.3: Values for the WLF constants for both the NSFBF and LSFBF fluids.

	c_1	c_2	R^2
NSFBF	11.33	-7638	0.94
LSFBF	0.025	-6.87	1

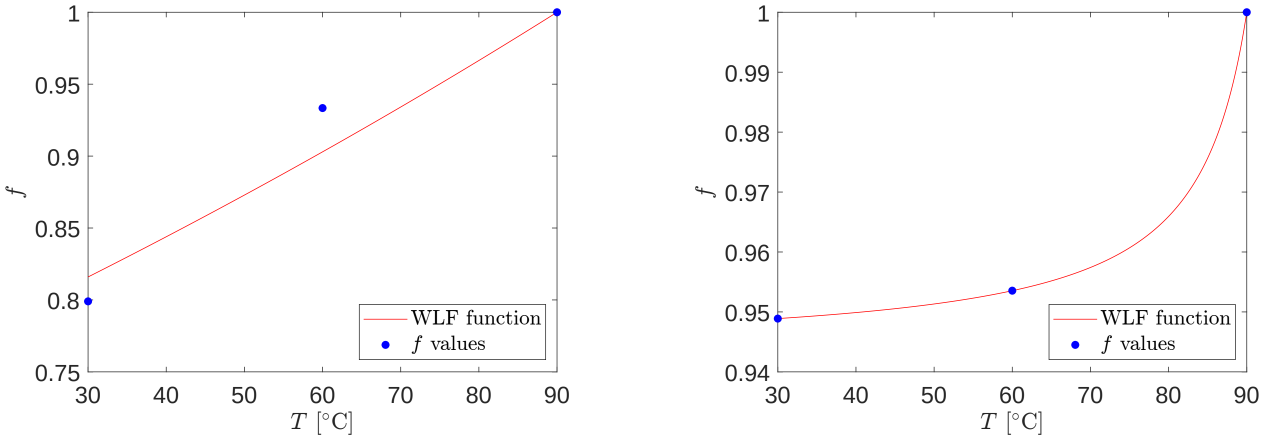

(a) NSFBF

(b) LSFBF

Figure 2.3: Plot of the values from Table 2.2 as well as the best Williams-Landel-Ferry (WLF) curves to fit them.

In addition to the viscosity of the fluid described above, the remaining fluid properties will be the same among the three fluids considered. This is because both NSFBF and LSFBF are water-based fluids. Thus, properties such as density, for instance, exhibit minimal variation from water and can be considered equivalent. Other properties considered in this work were:

- Density: $\rho = 1000$ kg m^{-3}
- Specific heat capacity: $c_P = 4186$ J kg^{-1}
- Thermal conductivity: $k = 0.598$ W m^{-1} °C^{-1}
- Thermal expansion coefficient: $\beta = 0.000210$ °C^{-1}

2.2 Numerical method

2.2.1 Governing equations

Fluid flow is dictated by a set of differential equations. In the current scenario, the flows are characterized as incompressible, transient, laminar, single-phase, and non-isothermal. To fully understand flow behavior, three governing equations must be solved: the conservation of mass (continuity equation), the conservation of momentum, and the conservation of energy [26]. These equations are as follows:

- Mass conservation

  The principle of mass conservation dictates that the mass cannot be created or destroyed. Therefore, in an open system, the mass entering minus the mass leaving must be equal to the change in mass within that system. For an incompressible flow, the equation for mass conservation is as follows:

  $$\nabla \cdot \mathbf{u} = 0, \tag{2.9}$$

  where $\mathbf{u}$ is the fluid velocity vector.

- Momentum conservation

  The conservation of momentum is governed by Newton's second law of motion, expressed as $\mathbf{f} = m \cdot \mathbf{a}$, where $\mathbf{f}$ represents the sum of all forces acting on the body, and $\mathbf{a}$ is the acceleration vector. In a broader context, this equation can be conceptualized as follows: the rate of increase in momentum within a volume is equivalent to the net inflow of momentum plus the net force exerted within that volume [27]. For incompressible fluid flow, this equation can be written as:

  $$\rho \left(\frac{\partial \mathbf{u}}{\partial t} + \mathbf{u} \cdot \nabla \mathbf{u} \right) = -\nabla p + \nabla \tau + \mathbf{f}, \tag{2.10}$$

  where ρ is the fluid density, p is the pressure and $\mathbf{f}$ is the sum of all external forces such as gravity. In addition, τ is the extra stress tensor which for a GNF can be given by Equation (2.2), with the shear rate ($\dot{\gamma}$) being equal to $\frac{1}{2}\left(\nabla \mathbf{u} + \nabla \mathbf{u}^{\mathrm{T}}\right)$.

  In non-isothermal flows, even though the flow is considered incompressible, natural convection can still be considered without excessively complicating the momentum equation. To facilitate this, the Boussinesq approximation can be applied. This approximation provides the density value (ρ') for varying temperatures using the thermal expansion coefficient:

  $$\rho' = \rho \left[1 - \beta \left(T - T_{\mathrm{ref}} \right) \right]. \tag{2.11}$$

  Using this approximation, the momentum equation can be modified to Equation (2.12) by adding the effects of natural convection.

$$\rho\left(\frac{\partial \mathbf{u}}{\partial t}+\mathbf{u}\cdot\nabla\mathbf{u}\right)=-\nabla p+\nabla\tau+f+\rho'\mathbf{g}. \tag{2.12}$$

It is also important to note that while adding the natural convection to the momentum equation makes the model more robust, for a lot of polymers, especially with flows at high viscosity, the effects of natural convection are minimal.

- Energy conservation

  Similarly to mass and momentum, energy is subject to conservation as dictated by the first law of thermodynamics. Although energy can undergo transformations from one form to another, the total amount of energy within a system remains constant. For incompressible fluids, the energy conservation equation can be written as follows:

$$\rho c_P\left(\frac{\partial T}{\partial t}+\mathbf{u}\cdot\nabla T\right)=\nabla\cdot(k\nabla T)+\tau:\nabla\mathbf{u}+S_T+R_T, \tag{2.13}$$

  where S_T is the volumetric source of energy, R_T is the heat transferred by radiation, which in this case was not considered, c_P is the specific heat capacity, k is the thermal conductivity and : is the double inner product operation.

2.2.2 Finite volume method

In computational fluid dynamics (CFD), the governing equations are discretized over a grid in order to obtain a numerical solution that would have been impossible for a lot of cases using an analytical method. There are several ways to discretize the equations, with the most popular being: the finite differences method (FDM), the finite element method (FEM) and the finite volume method (FVM). The FDM is the simplest among the three and is relatively straightforward to implement on a regular grid. However, it introduces numerous challenges when applied to irregular grids [28]. Consequently, many modern CFD solvers opt for FEM or FVM. The OpenFOAM framework used in this work employs the FVM.

In the FVM discretization the governing equations are integrated over the volumes or cells to obtain a linear system of equations, which is solved to obtain the values of each variable in each cell centroid. In addition, this method involves transforming certain terms within the conservation equation into face fluxes. The flux is conserved in a volume because any flux entering a cell is the same as the flux leaving the previous cell. This property makes FVM as the preferred approach in CFD while FEM is more commonly used in solid mechanics. In addition to that, because variables are evaluated in the center of cells rather than at the edges, implementing boundary conditions is less intrusive [29].

The discretization process consists of four steps:

- Step 1: Create the geometry and the physical model.

  This step consists of transforming the real-life physical problem into a model. For that purpose, the geometry and boundary conditions are created. The details of this process are explained in Chapter 3.

- Step 2: Geometry discretization.

  In this step, the mesh is created to discretize the geometry into a finite number of volumes. The quality of the mesh is also assessed to create the best discretization possible. This process is also explained in Chapter 3.

- Step 3: Equation discretization

  In this step, the previously mentioned differential governing equations are discretized into algebraic equations for computation within the mesh elements.

  This process depends on the chosen grid. An illustration of a grid is provided in Figure 2.4.

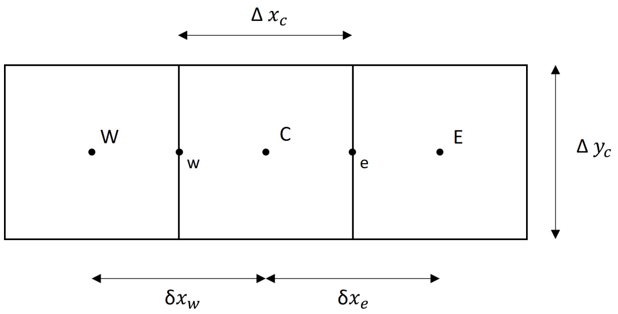

Figure 2.4: Example of a one dimension grid. Adapted from Moukalled *et al.* [29].

The momentum conservation equation (Equation 2.12) can be discretized as Equation 2.14 with the exception of the pressure term, since it does not have a specific equation to calculate. To obtain both the pressure and the velocity fields, an algorithm like SIMPLE (Semi-implicit Method for Pressure-Linked Equations) can be used.

$$(\rho u \Delta y)_e u_e - (\rho u \Delta y)_w u_w = \left(\eta_e \frac{\partial u}{\partial x} \Delta y\right)_e - \left(\eta_w \frac{\partial u}{\partial x} \Delta y\right)_w - \int \frac{\partial p}{\partial x} dA. \tag{2.14}$$

The continuity equation is simpler than the conservation of momentum and thus can be discretized, for instance, for a one-dimensional grid into:

$$(\rho u \Delta y)_e - (\rho u \Delta y)_w = 0. \tag{2.15}$$

- Step 4: Solution of the equations

  Finally, in this section, the algebraic equations are solved for each of the elements using an iterative process [29].

Chapter 3

Case study

After the fluid was characterized, the next phase involved designing the geometry of the EGS domain. As described in Section 1, EGS typically operates by drilling two wells and flowing fluid between them. However, there are other geometries that can be explored. One such technology is the Downhole Heat Exchanger (DHE) also known as a single-well geothermal system. In this approach, only one well is used and the fluid circulates within two concentric cylinders [30]. This was the geometry used in the present simulations.

3.1 Geothermal system geometry

The geometry designed for the simulations was inspired by that studied in Bu *et al.* [31]. A schematic representation of the geometry of the geothermal system can be seen in Figure 3.1.

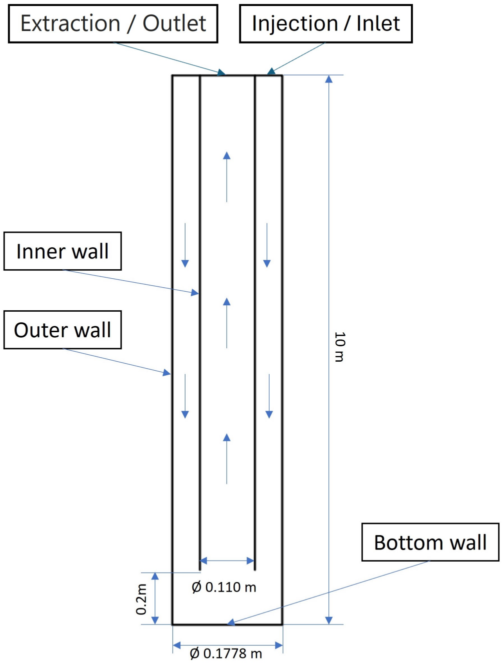

Figure 3.1: Representation of a single-well geothermal system. Adapted from Bu *et al.* [31].

One challenge encountered during the geometric creation process was the discrepancy in the depth of the well. Although in Bu *et al.* [31] the depth of the well was 2650 m, trying to generate a geometry and mesh for a DHE of such proportions proved problematic. This is because, for a geometry with that length and only 177.8 mm in diameter, to obtain an accurate solution in the cross section of the geometry, the number of elements in the direction z would have to be very large. Due to limited computational resources, this option was not feasible. As a pragmatic solution, the decision was to reduce the well length to 10 m while adjusting the thermal gradient accordingly so that the temperature difference between the top and bottom of the DHE would show meaningful results. Despite this modification, the injection temperature and velocity remained consistent with those of the original work [31].

The geometry of the geothermal system was created using FreeCAD software [32] and then imported into OpenFOAM. The geometry surface was divided into five sections, each representing a different boundary condition, as follows:

- Inlet - Both the values of temperature and velocity were set for the inlet and remain constant through the simulation.
- Outlet - The boundary condition at the outlet was a fixed value of zero for the pressure field. The velocity here is unknown and will be calculated in the simulation.
- Inner wall - The velocity of the fluid diminishes near the inner wall, adhering to the no-slip condition, resulting in a velocity of zero at this boundary. In addition, the inner wall acts as a thermal insulator, preventing heat transfer. This ensures that the fluids circulating up and down the well remain isolated in terms of heat exchange.
- Outer wall - Similar to the inner wall, the fluid velocity is zero at the outer wall. However, the temperature was set along this boundary, with a non-uniform distribution across the wall. Specifically, at the top near the inlet, the wall temperature matches the inlet temperature. Subsequently, a temperature gradient was established along the wall. Various simulations with different temperature gradients were conducted to compare the results.
- Bottom wall - Like the other walls, the velocity here is zero and the temperature was set so that it is equal to that at the bottom of the outer wall.

3.2 Mesh generation

The mesh used to discretize the domain was generated using the cfMesh software. The specified parameters included a maximum cell size of 100 mm and a minimum cell size of 20 mm. With these settings, the mesh could be generated, but an issue arises at the bottom of the inner wall. To address this, a local refinement was applied specifically in that region. In addition to that, a refinement was also applied at the outlet and inlet patches to obtain accurate results when measuring the average temperature during the simulations. In all these refinements, the chosen cell size was 5 mm.

Figure 3.2 shows the problem in the inner wall of the mesh that was addressed by local refinement.

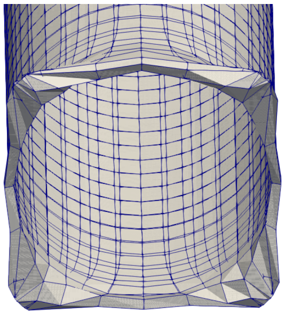

Figure 3.2: Mesh at the bottom of the inner wall before the local refinement.

Following the implementation of these refinements, the updated mesh is shown in Figure 3.3. A cross-sectional view of the mesh, illustrated in Figure 3.3b, clearly highlights the refined zone.

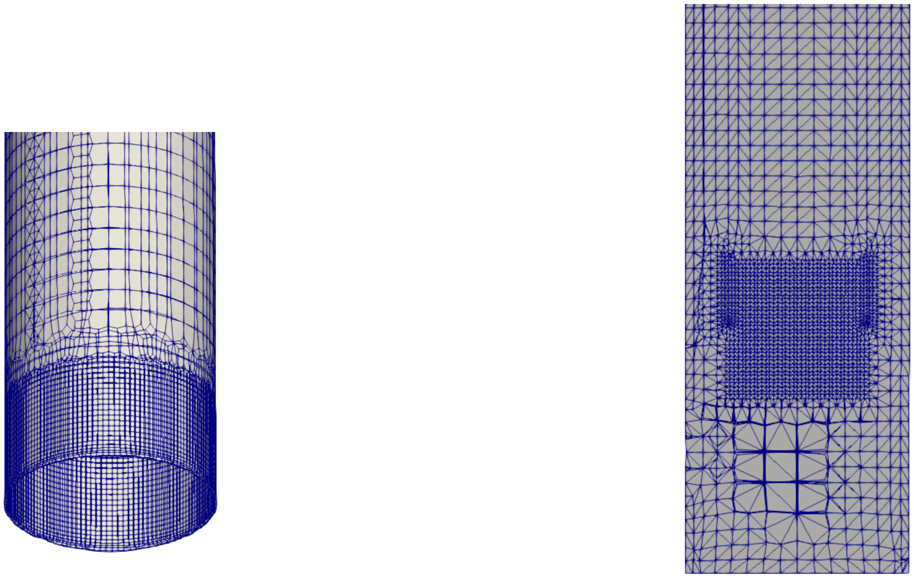

(a) View of the mesh in the inner wall.

(b) Slice of the mesh.

Figure 3.3: Mesh at the inner wall after the local refinement was used.

In addition to the inner wall, the inlet and outlet patches also received a local refinement. The result can be seen in Figure 3.4.

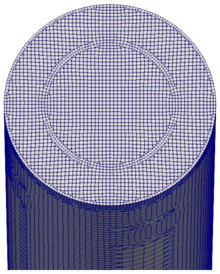

Figure 3.4: Section of the mesh at the top of the geometry.

In order to assess the quality of the mesh, some parameters were calculated. These parameters are:

- Number of cells: 413352;
- Average number of faces per cell: 6.12084;

  Given that the mesh is hexahedrical, an acceptable average number of faces per cell should be around six.
- Maximum aspect ratio: 7.97838;

  The aspect ratio is defined as the ratio between the longest and shortest sides of a cell [33]. Acceptable values for the maximum aspect ratio vary depending on the specific geometry, and in certain situations, aspect ratios up to 1000 could even be considered acceptable.

  Since the cells in this mesh were tried to be regular hexahedrons, a small aspect ratio would be preferred. Therefore, the obtained value of 7.97838 falls within an acceptable range.
- Mesh non-orthogonality - Max: 60.9328 average: 5.54928;

  Non-orthogonality corresponds to the angle (in degrees) between a vector connecting the center of two adjacent cells and the normal vector of the face between those cells. If the mesh is regular and aligned with the Cartesian grid, the non-orthogonality is going to be zero. Although the overall average non-orthogonality in the created mesh is not very high, certain cells exhibited elevated values. In such cases, non-orthogonal correctors were applied to enhance the accuracy of the simulation [34].
- Maximum skewness: 3.30974;

  Skewness is the deviation of the vector connecting the center of two adjacent cells and the center of the face between the two cells. In Figure 3.5, this deviation corresponds to the distance between f and f'.

  The maximum skewness value obtained for the generated mesh is somewhat elevated at 3.30974, but it still falls within an acceptable range. OpenFOAM typically considers a threshold of four for an acceptable maximum skewness value, and in this context, the created mesh is deemed acceptable.

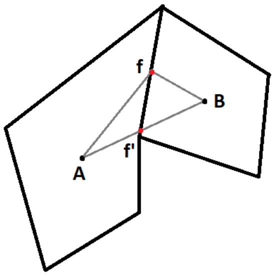

Figure 3.5: Two adjacent cells in the mesh. Adapted from Moukalled *et al.* [29].

3.3 Simulation parameters

The injection temperature of the fluid was set at 5 °C and the inlet velocity of the injected fluid was considered 0.7174 m/s. The wall temperature gradient was set at three different values depending on the simulation: 5 °C, 10 °C and 50 °C, all along the 10 m height of the well, rather than the real thermal gradient of 27.8 °C/km imposed in the geothermal field operations.

In the OpenFOAM simulations, the RheoTool library was employed, offering solvers designed for non-Newtonian fluid flows. Specifically, the *rheoHeatFoam* solver was used because of its suitability for non-isothermal simulations. Since the solver uses an iterative process, the tolerance for the residuals of the dependent variables was set as follows:

- Tolerance for pressure = 10^{-7};
- Tolerance for velocity = 10^{-6};
- Tolerance for temperature = 10^{-6}.

Due to the relatively high non-orthogonality, non-orthogonal correctors were applied in the simulations. Specifically, two correctors were used in the water simulations, while three were employed in the non-Newtonian simulations.

For the pressure-velocity coupling algorithm, the SIMPLEC (Semi-Implicit Method for Pressure Linked Equations-Consistent) method was utilized. This algorithm is similar to SIMPLE but more suitable for transient fluid flows at low Reynolds numbers in terms of stability and accuracy [26]. In OpenFOAM, the tolerance specifications, the number of non-orthogonal correctors, and the solution algorithm are stored in a file called *fvSolution*.

Another important file that must be created is the file containing the simulation controls, the *ControlDict* file. The most important parameters to introduce are the total simulation time and the duration of each time-step. Each simulation was run until the steady state was reached. The duration of each time-step is important because it is used to calculate the Courant number (Co) given as follows:

$$Co = \frac{u\Delta t}{\Delta x} \tag{3.1}$$

where Δt is the time-step duration and Δx is the length of the cell. This means that Co is calculated for every cell. It is generally recommended to maintain Co below the value of 1 for stability. In OpenFOAM, it is possible to set a value for the maximum Co that should be achieved rather than setting a specific value for Δt. In the simulations performed in this work we follow this procedure. Initially, when pressure and velocity values undergo significant variations, the maximum Co was set to 1. After simulating around 0.1 seconds of the flow, this value was adjusted to 5. Although 5 may seem large, only a few cells approached this value. Keeping the maximum Co at 5 for the majority of the simulation duration effectively maintained an average Co around 0.8 to 1.

Chapter 4

Results and discussion

To compare the use of thermo-thickening fluids (NSFBF and LSFBF) with the use of a Newtonian fluid (water) in a single-well geothermal system, simulations were conducted at different temperature differences (ΔT) imposed in the vertical direction of the well (that is, the difference between the top and bottom temperatures), specifically 5 °C, 10 °C and 50 °C.

4.1 Newtonian fluid

All simulations started with water within the well at an initial temperature value of 5 °C and converged to a steady-state where the average temperature at the outlet reached a constant value. The variation in the average temperature at the outlet over time for different ΔT is shown in Figures 4.1 to 4.3 as well as the steady-state temperature contour in a frontal plane near the bottom of the well.

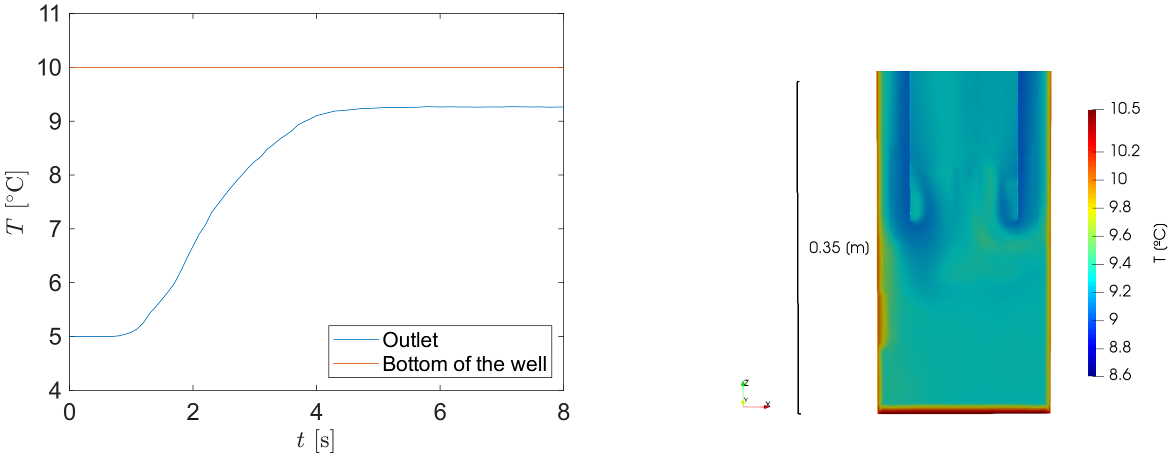

(a) Evolution of the average temperature at the outlet over time.

(b) Steady-state temperature contour in a frontal plane near the bottom of the well.

Figure 4.1: Results for the downhole heat exchanger process filled with water subjected to a temperature difference of 5 °C.

In steady state, the average temperature at the outlet is lower than that imposed at the bottom boundary of the well. This outcome is expected because the temperature naturally decreases with increasing distance from the heat source. This phenomenon can be seen in Figures 4.1b, 4.2b and 4.3b. The values of the average temperature in the outlet and bottom boundaries in steady-state can be seen in Table 4.1, as well as the difference between them. As the temperature at the bottom boundary increases, the difference between the average

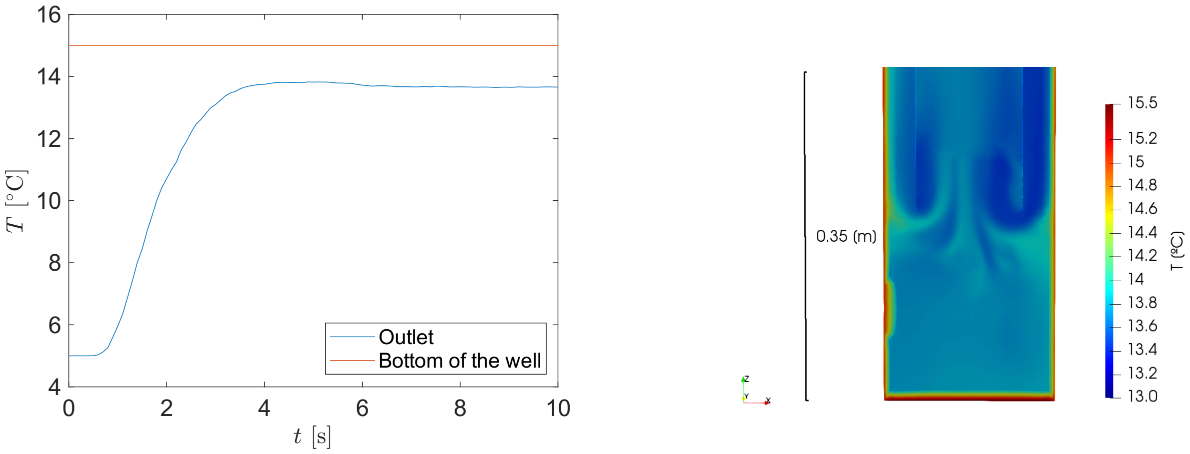

(a) Evolution of the average temperature at the outlet over time.

(b) Steady-state temperature contour in a frontal plane near the bottom of the well.

Figure 4.2: Results for the downhole heat exchanger process filled with water subjected to a temperature difference of 10 °C.

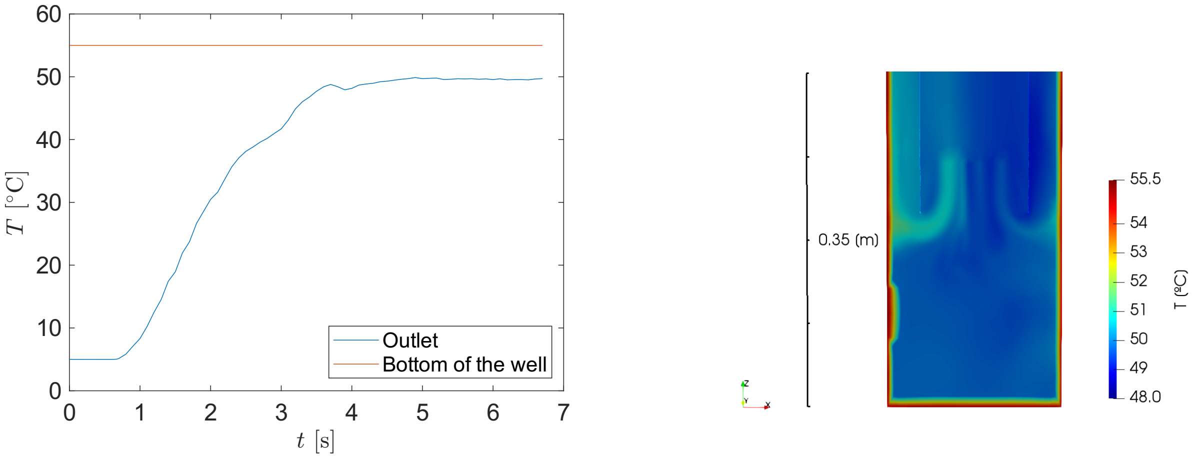

(a) Evolution of the average temperature at the outlet over time.

(b) Steady-state temperature contour in a frontal plane near the bottom of the well.

Figure 4.3: Results for the downhole heat exchanger process filled with water subjected to a temperature difference of 50 °C.

temperature at the outlet and the temperature at the bottom boundary also increases. These results allow us to conclude that the average temperature at the outlet is similar to the imposed values at the bottom boundary of the DHE. This indicates that for simple geometries such as the single DHE, water remains a viable choice as a geothermal fluid.

In addition to the temperature field, analysis of the velocity profile provides further insight into the dynamics of the well. The velocity profile was calculated for two distinct heights within the well: one immediately after the fluid enters the ascending section ($z = 0.25$ m) and another at the middle line ($z = 5$ m) of the well where the flow has already developed. Figure 4.4 shows these velocity profiles, as well as the steady-state velocity contour in a frontal plane near the bottom of the well for a temperature difference of 5 °C. In Figure 4.4a it can be seen that the velocity values at $z = 0.25$ m are higher than those at $z = 5$ m. This observation

Table 4.1: Comparison between the outlet and the bottom (imposed) temperature values in steady-state.

		T outlet [°C]	T bottom [°C]	Difference [°C]
ΔT [°C]	5	9.3	10	0,7
	10	13.7	15	1,3
	50	49.7	55	5,3

is supported by Figure 4.4b, where the fluid reaches its highest velocity at the entrance of the ascending section, which decreases thereafter. The profiles differ in magnitude and also exhibit variations in shape. At $z = 0.25$ m, the profile is notably irregular, even showing a minor recirculation of the flow near the inner wall on the right side of the domain. This effect can be attributed to the sudden change in the flow direction. In contrast, at $z = 5$ m, the velocity profile is more uniform. Due to water's low viscosity ($\mu = 0.001$ kg m^{-1} s^{-1}), the viscous effects near the wall are minimal, allowing the maximum velocity in the developed flow ($u_z = 8$ m/s) to be achieved across most points in the cross-section.

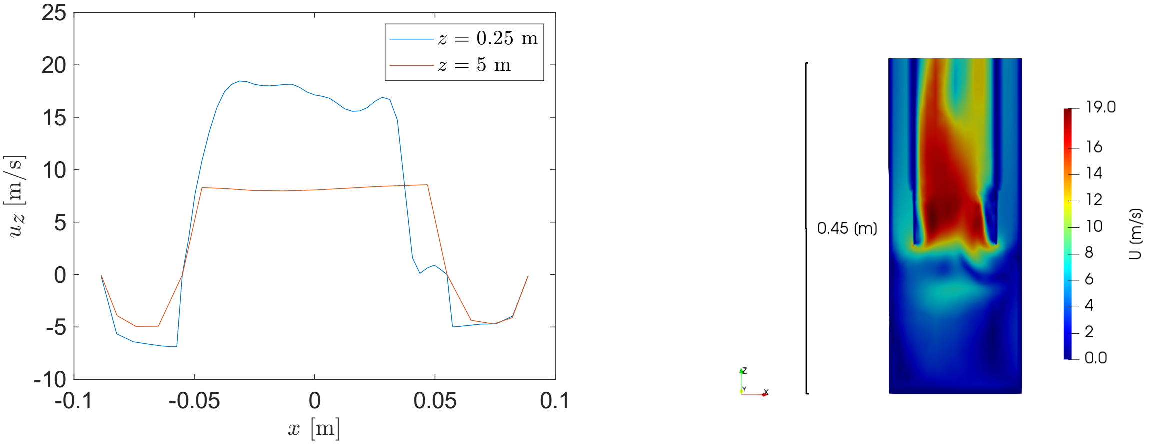

(a) Steady-state velocity profiles at two different heights of the well.

(b) Steady-state velocity contour in a frontal plane near the bottom of the well.

Figure 4.4: Results for the velocity field in the downhole heat exchanger process filled with water subjected to a temperature difference of 5 °C.

In Figures 4.5 and 4.6 the velocity profiles for the remaining two temperature differences ($T = 10$ °C and $T = 50$ °C) are presented. When comparing these two figures with Figure 4.4a, a clear correlation emerges: velocity values increase with the temperature difference, particularly in the developing flow at $z = 0.25$ m. Furthermore, more pronounced recirculations are revealed at the entrance of the ascending section, as evidenced by Figure 4.6.

Lastly, we evaluated the pressure field in the well. The pressure values were measured along a vertical line with a length equal to the height of the well $h = 10$ m, that is, from the bottom to the top of the well. Figures 4.7 to 4.9 show the variation of the pressure for different temperature differences. It should be noted that the property measured along this line is the static pressure (p) subtracted by the contribution of hydrostatic pressure ($\rho'(\mathbf{g}\cdot\mathbf{h})$) [26], given by

$$p_{rgh} = p - \rho'(\mathbf{g}\cdot\mathbf{h}), \tag{4.1}$$

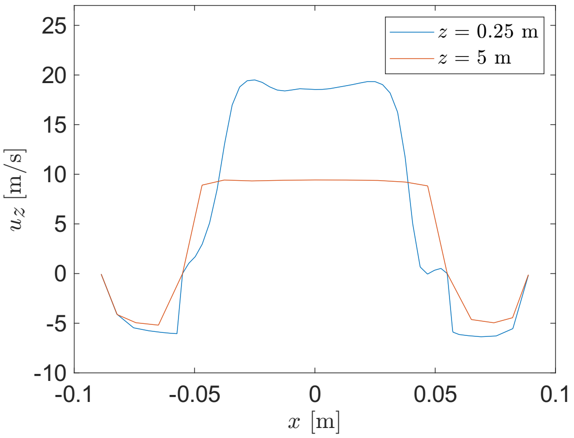

Figure 4.5: Steady-state velocity profiles at two different heights in the downhole heat exchanger process filled with water subjected to a temperature difference of 10 °C.

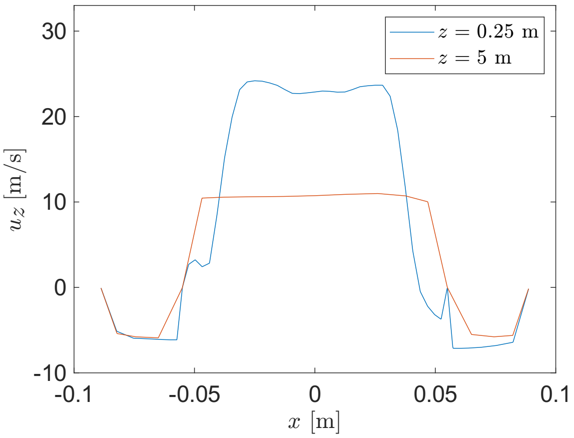

Figure 4.6: Steady-state velocity profiles at two different heights in the downhole heat exchanger process filled with water subjected to a temperature difference of 50 °C.

where ρ' is the density value obtained from the Boussinesq approximation (Equation 2.11), $\mathbf{g}$ is the gravity and h is the position vector of the cells center. It is evident that in all scenarios the pressure decreases with increasing height, reaching $p_{rgh} = 0$ when $h = 10$ m. This decrease aligns with expectations, as the viscous effects induced by fluid flow in a pipe contribute to friction, leading to a further decrease in pressure: a phenomenon quantified by the Darcy–Weisbach equation [35].

In Figures 4.7 to 4.9, in addition to illustrating the variation in pressure along the height of the well, a focused view of the pressure changes is presented for $0 \leq h \leq 1$ m. Although pressure exhibits a predominantly linear variation with height over a span of 10 m, in this specific region, a substantial pressure drop is found. This behavior can be attributed to the transition zone, where the fluid exits the descending region of the well and enters the ascending region, causing a sudden change in the direction of the velocity and consequent pressure reduction. This phenomenon becomes less pronounced as the temperature difference increases.

An important observation regarding pressure results is that Figures 4.7 to 4.9 capture specific moments in time, 8 s, 10 s and 6.5 s, respectively. To understand how pressure evolves over time, the pressure difference between the medium pressure at the inlet and outlet was plotted against time. Furthermore, the pressure difference between the bottom of the well and the outlet can also be visualized. Figure 4.10 shows the results of the pressure differences obtained for the case with a temperature difference of 5 °C. Upon examining the figure, it becomes evident that the pressure does not reach a steady-state. However, despite the pronounced fluctuations in pressure at the inlet and the bottom of the well, there exists a constant ratio between them, expressed as:

$$\frac{\Delta p_{inlet}}{\Delta p_{bottom\ of\ the\ well}} = \frac{p_{inlet} - p_{outlet}}{p_{bottom\ of\ the\ well} - p_{outlet}} \approx 1.46. \tag{4.2}$$

Furthermore, even though the pressure values at the bottom of the well show temporal variations, the curves illustrated in Figures 4.7 to 4.9 remain consistent despite alterations

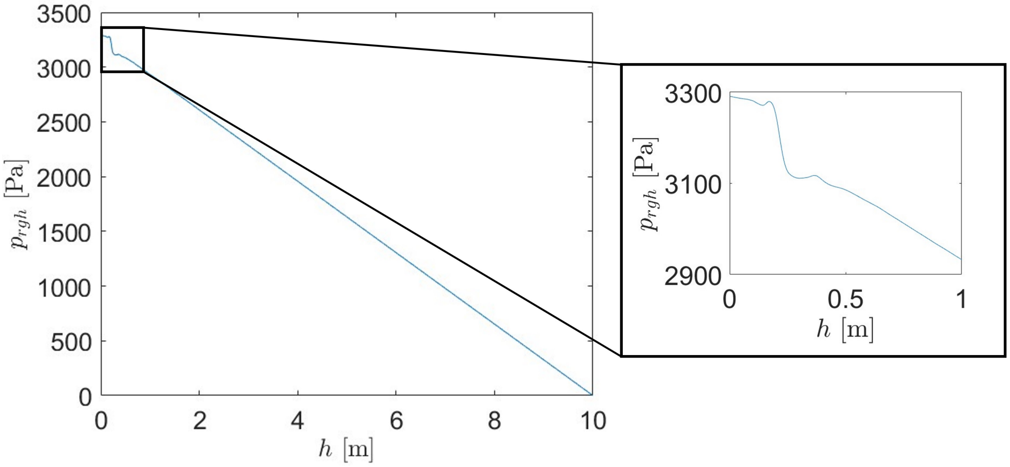

Figure 4.7: Pressure variation along the well height in the downhole heat exchanger process filled with water subjected to a temperature difference of 5 °C, at time equal to 8 s.

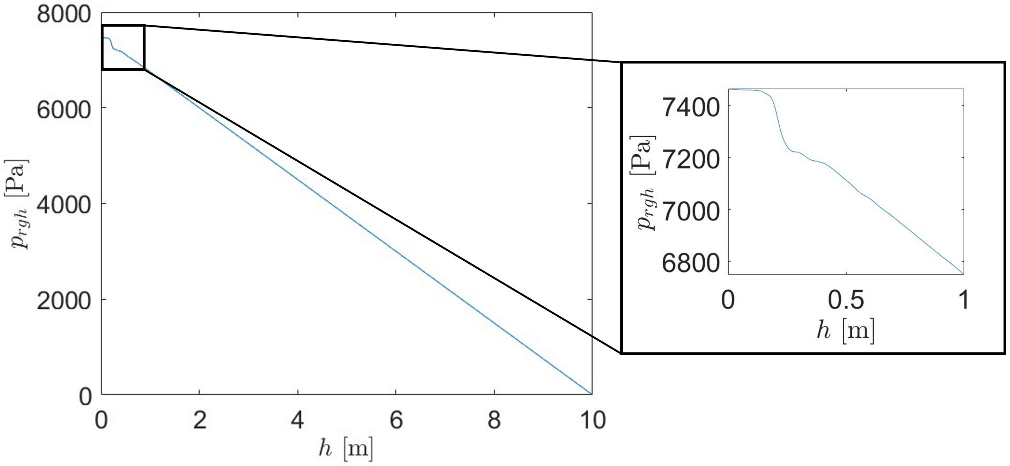

Figure 4.8: Pressure variation along the well height in the downhole heat exchanger process filled with water subjected to a temperature difference of 10 °C, at time equal to 10 s.

in the chosen time instance always showing the highest pressure drop around $h = 0.25$ m.

4.2 Non-solid freshwater base fluid (NSFBF)

In contrast to the Newtonian scenario in which a single simulation was performed for each temperature difference, in the current study, two simulations were performed for each difference. In the first simulation, the fluid was assumed to exhibit viscosity based on a Herschel-Bulkley model and to be constant across temperatures. In the second simulation, the WLF multiplicative function was used to take into account changes in viscosity as a result of temperature. Figures 4.11a, 4.12a and 4.13 show the comparison of the evolution of the average temperature at the outlet over time for the non-Newtonian NSFBF fluid.

In these figures, the comparison between the outlet temperature in the steady-state of

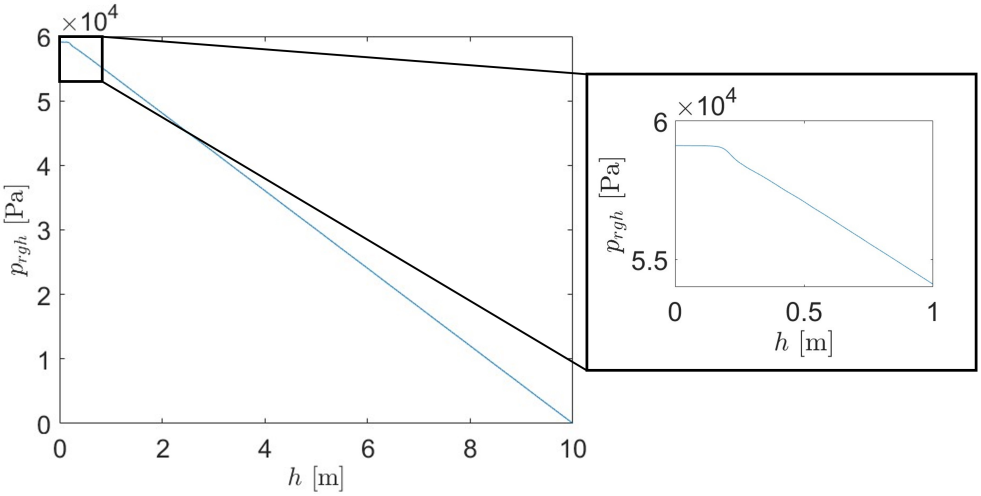

Figure 4.9: Pressure variation along the well height in the downhole heat exchanger process filled with water subjected to a temperature difference of 50 °C, at time equal to 6.5 s.

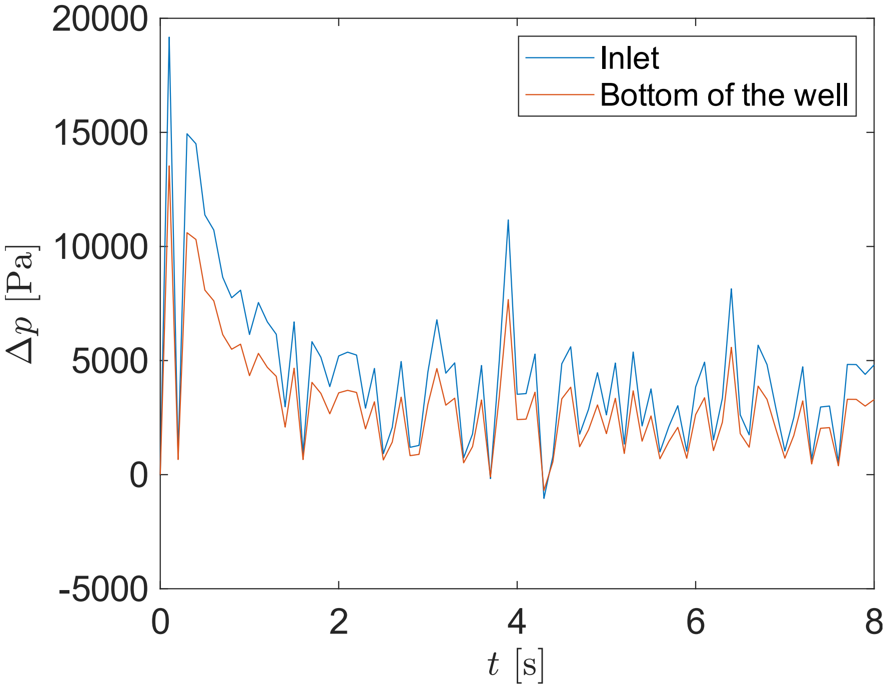

Figure 4.10: Variation of the pressure difference over time in the downhole heat exchanger process filled with water subjected to a temperature difference of 5 °C.

a nonthermo-thickening fluid (without the WLF model) and a thermo-thickening fluid (with the WLF model) can be seen. When examining lower temperature differences in the well (Figures 4.11a and 4.12a), it becomes apparent that the average temperature at the outlet is higher in the thermo-thickening fluid. This observation suggests that the thermo-thickening effect contributed to a more favorable geothermal energy extraction. On examination of Figure 4.13a, it becomes evident that the thermo-thickening fluid now has an efficiency similar to that of the nonthermo-thickening fluid in geothermal energy extraction (see the zoomed

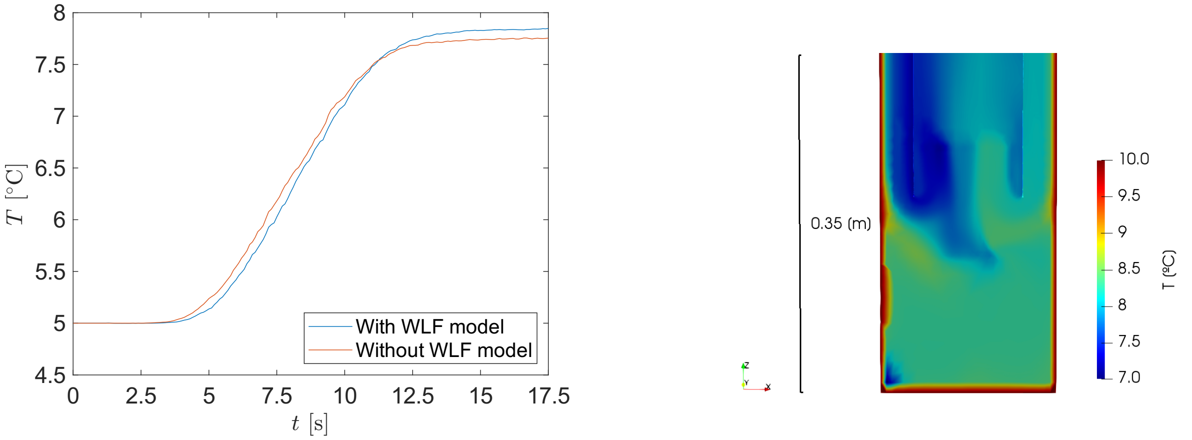

(a) Evolution of the average temperature at the outlet over time.

(b) Steady-state temperature contour in a frontal plane near the bottom of the well.

Figure 4.11: Results for the downhole heat exchanger process filled with a non-solid freshwater base fluid (NSFBF) subjected to a temperature difference of 5 °C.

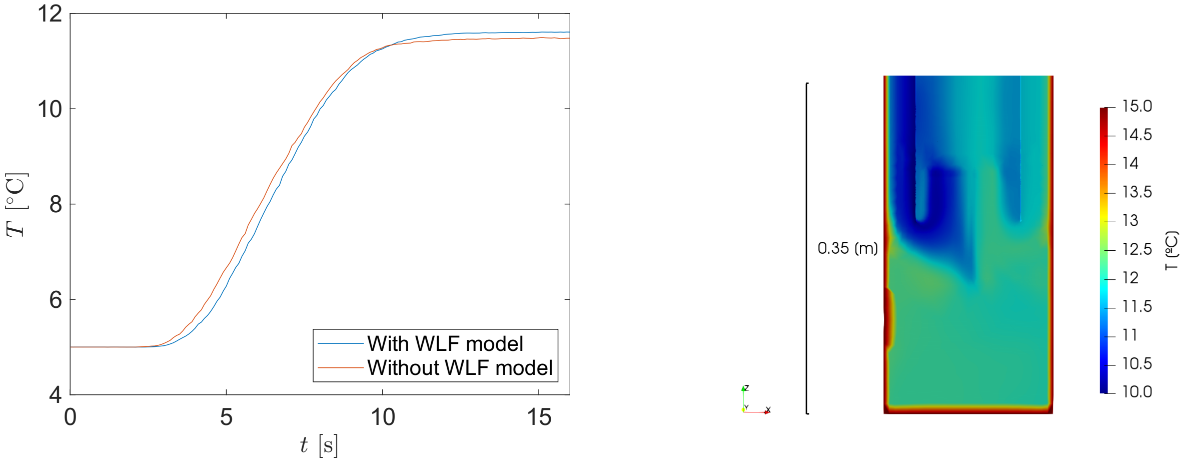

(a) Evolution of the average temperature at the outlet over time.

(b) Steady-state temperature contour in a frontal plane near the bottom of the well.

Figure 4.12: Results for the downhole heat exchanger process filled with a non-solid freshwater base fluid (NSFBF) subjected to a temperature difference of 10 °C.

time interval shown in Figure 4.13b). From this observation, one could theorize that the thermo-thickening effect is more pronounced for lower temperature gradients. In this way, the thermo-thickening effect was generally considered beneficial, and subsequent analyses were conducted with this effect taken into account. Similarly to the previous scenario, the outlet temperature remains lower compared to the temperature imposed at the bottom of the well. As the distance from the bottom increases, there is a general trend for a decrease in temperature. However, this reduction is not uniform, especially as the flow transitions from the outer cylinder to the inner one. Significant changes in temperature occur because the fluid closest to the rock walls tends to be much hotter.

Figures 4.11b, 4.12b and 4.14a show the contour of the temperature distribution within the well near the bottom boundary. High temperatures are evident near the rock walls, but a

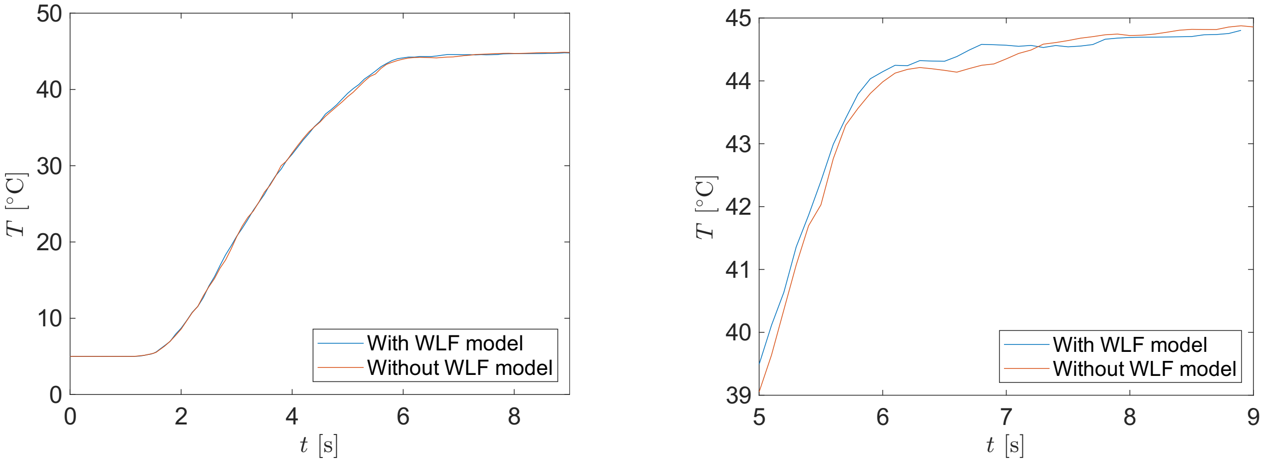

(a) Evolution of the average temperature at the outlet over time.

(b) Zoomed interval (last 4 seconds) of the average temperature at the outlet.

Figure 4.13: Results for the downhole heat exchanger process filled with a non-solid freshwater base fluid (NSFBF) subjected to a temperature difference of 50 °C.

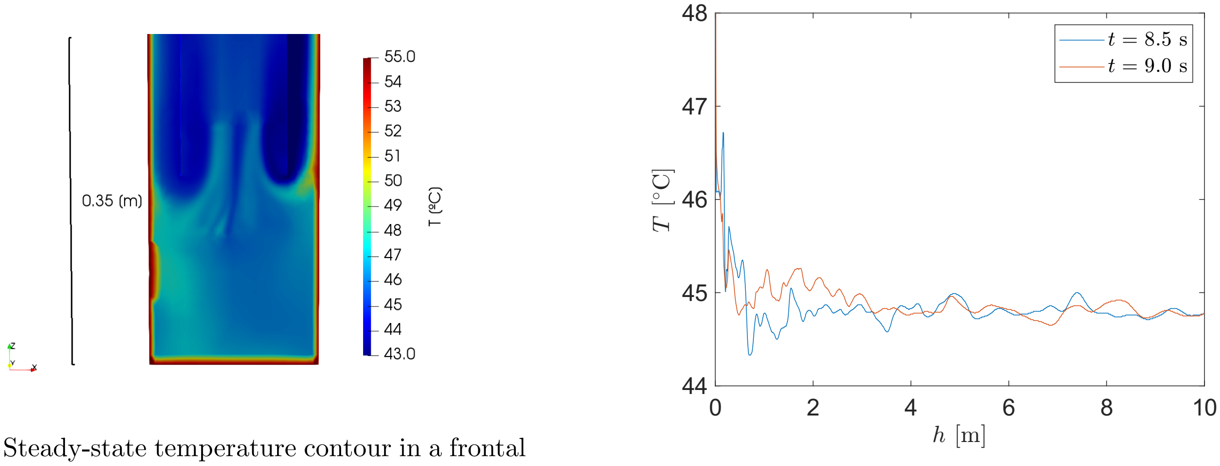

(a) Steady-state temperature contour in a frontal plane near the bottom of the well.

(b) Temperature variation along the well height.

Figure 4.14: Spatial variation of temperature for the downhole heat exchanger process filled with a non-solid freshwater base fluid (NSFBF) subjected to a temperature difference of 50 °C.

rapid reduction occurs just a few centimeters away from them. This explains the slow heating until steady-state, as well as the difference between the outlet temperature and the bottom temperature when steady-state is reached.

The temperature profiles for different time moments, $t = 8.5$ s and $t = 9.0$ s, are shown in Figure 4.14b. The fluid temperature was obtained along a vertical line normal to the bottom boundary of the well, along the channel height. The fluid temperature is observed to undergo a rapid decrease with increasing height until it reaches approximately 0.2 m, coinciding with the point where the inner wall begins. Beyond this point, the temperature stabilizes. Smaller temperature oscillations are seen near the outlet region, where geothermal extraction is performed.

Similarly to Section 4.1, the velocity profiles are also shown here for the NSFBF. Figure 4.15 show the results obtained for a temperature difference of 5 °C. Similarly to the water fluid, the velocity at the beginning of the ascending section ($z = 0.25$ m) for the non-Newtonian fluid surpasses that of the fully developed region ($z = 5$ m) as seen in Figure 4.15a. However, the developed velocity profile presents a different shape, and the maximum velocity occurs only at the midpoint, in contrast to the behavior observed with water. This deviation is attributed to the higher viscosity exhibited by the non-Newtonian fluid, when compared to that of water, which causes more friction and thus more kinetic energy is lost, leading to a more curved profile.

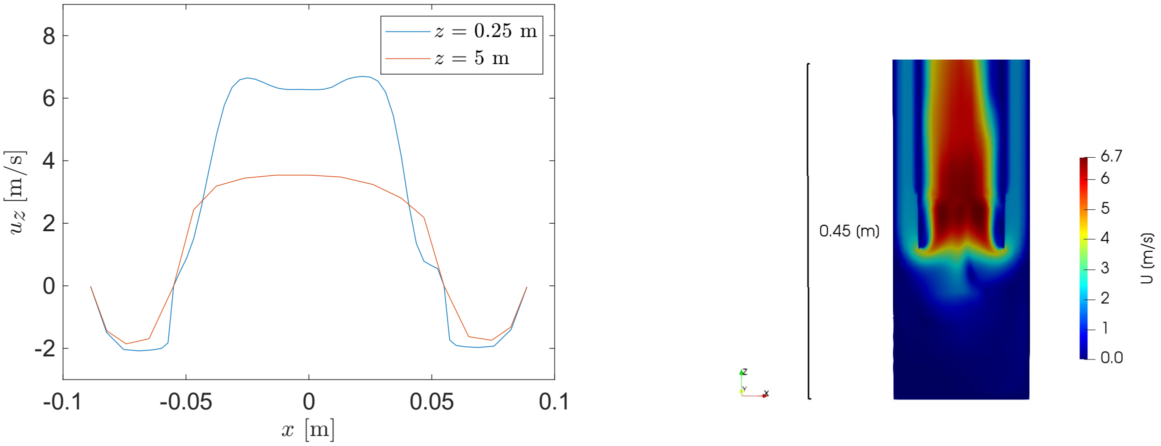

(a) Steady-state velocity profiles at two different heights.

(b) Steady-state velocity contour in a frontal plane near the bottom of the well.

Figure 4.15: Results for the velocity field in the downhole heat exchanger process filled with a non-solid freshwater base fluid (NSFBF) subjected to a temperature difference of 5 °C.

The resulting velocity profiles for the remaining temperature differences are presented in Figures 4.16 and 4.17. Once again, with an increase in the temperature gradient, both the velocity in the ascending region of the well and the recirculations at its entrance experience an increase. This phenomenon is particularly evident in Figure 4.17 where the velocity at the entrance of the ascending region reaches values of up to 14.61 m/s but also negative values of up to -1.40 m/s due to the recirculation of the flow.

Lastly, the pressure field is also analyzed for the NSFBF. Again, these results are obtained using the same vertical line as in Section 4.1. The results are presented in Figures 4.18 to 4.20. Similarly to water, the pressure variation exhibits a tendency to increase with an increase in the temperature difference. In addition, the pressure drop observed when the fluid enters the ascending region of the well is also evident here.

4.3 Low-solid freshwater base fluid (LSFBF)

Similarly to the previous case employing a NSFBF fluid, in this section, two simulations were made for each temperature difference. In the first simulation, the fluid's viscosity was presumed to adhere to the Herschel-Bulkley model, remaining constant across temperatures. In the second simulation, we incorporate the WLF multiplicative function to accommodate

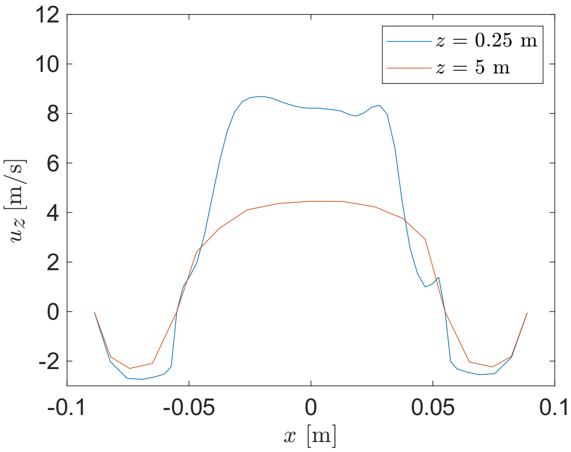

Figure 4.16: Steady-state velocity profiles at two different heights in the downhole heat exchanger process filled with a non-solid freshwater base fluid (NSFBF) subjected to a temperature difference of 10 °C.

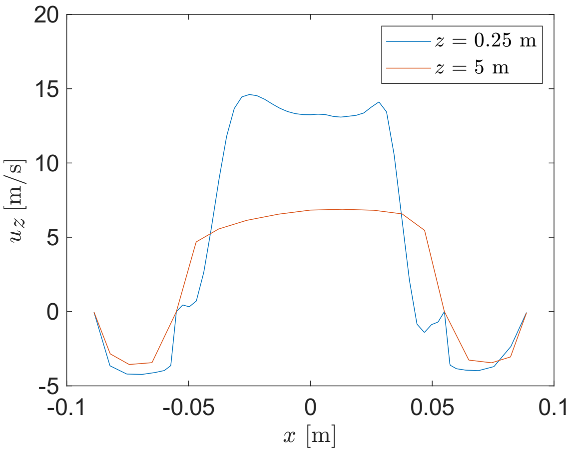

Figure 4.17: Steady-state velocity profiles at two different heights in the downhole heat exchanger process filled with a non-solid freshwater base fluid (NSFBF) subjected to a temperature difference of 50 °C.

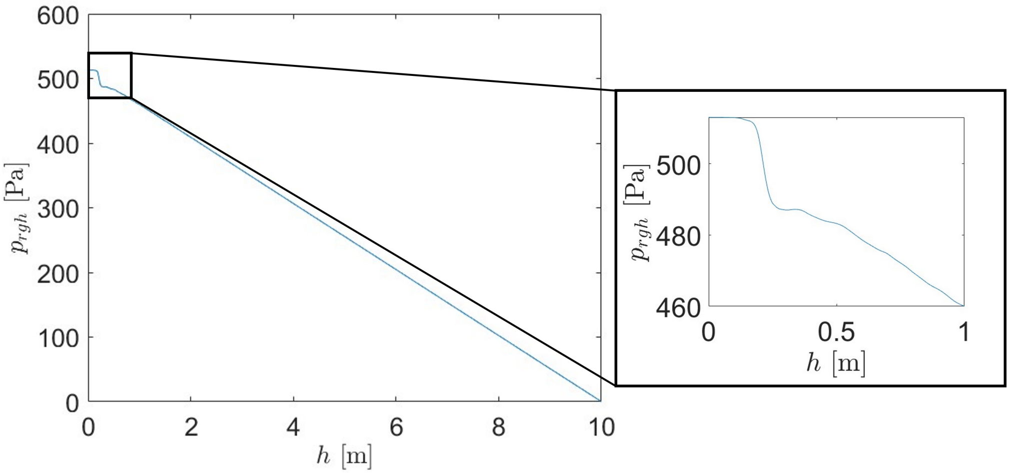

Figure 4.18: Pressure variation along the well height in the downhole heat exchanger process filled with a non-solid freshwater base fluid (NSFBF) subjected to a temperature difference of 5 °C, at time equal to 19 s.

variations in viscosity induced by temperature changes. The evolution of the average temperature at the outlet over time is shown in Figures 4.21a, 4.22a and 4.23a. In addition, Figures 4.21b, 4.22b and 4.23b show the contour of the temperature field in the frontal plane of the well in steady-state, where the temperature can be seen in the transition from the outer cylinder to the inner one. This time, the thermo-thickening effect was almost negligible, although it did contribute to a slight improvement of the results in the lower temperature gradients. Because the experimental fitting curve has an increasing derivative, it implies that temperatures below 30 °C show very similar viscosity values. Consequently, heating in this temperature range does not significantly alter the viscosity, thereby accounting for the minimal impact of the thermo-thickening effect. Due to this similarity, the two fluids studied in

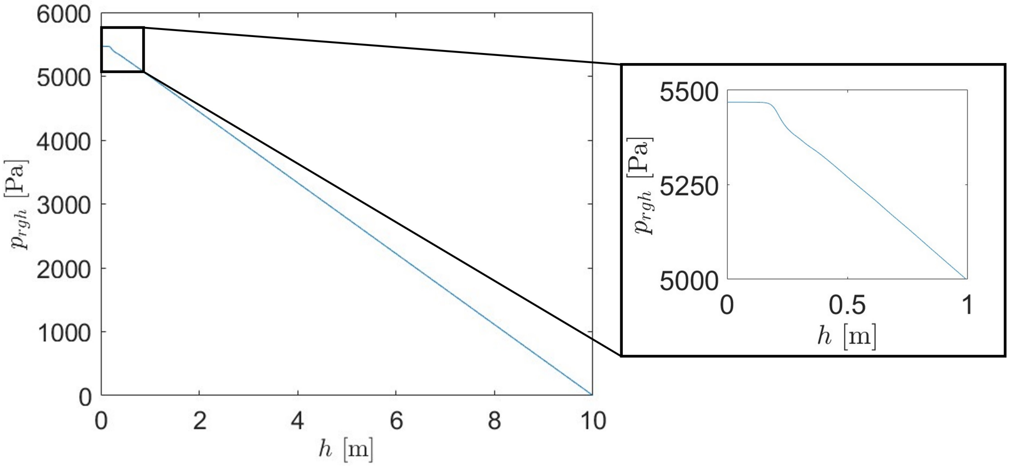

Figure 4.19: Pressure variation along the well height in the downhole heat exchanger process filled with a non-solid freshwater base fluid (NSFBF) subjected to a temperature difference of 10 °C, at time equal to 16 s.

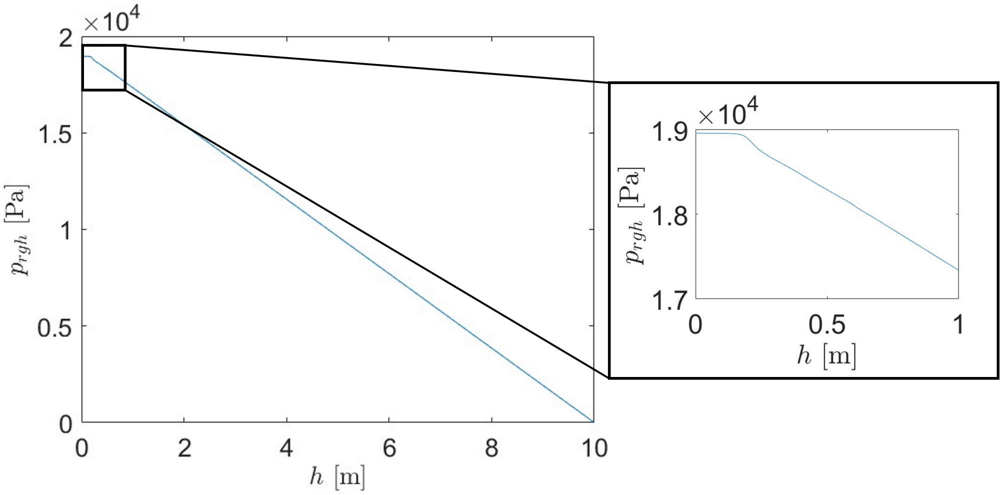

Figure 4.20: Pressure variation along the well height in the downhole heat exchanger process filled with a non-solid freshwater base fluid (NSFBF) subjected to a temperature difference of 50 °C, at time equal to 9.1 s.

this section exhibited nearly identical results. Therefore, subsequent analyses were conducted for the thermo-thickening fluid.

Figure 4.24 show the velocity profile at two different heights of the well along with the velocity contour plot in a frontal plane near the bottom of the well for a temperature difference of 5 °C. The resulting velocity profile shows a high resemblance to that of NSFBF, primarily because both fluids exhibit very similar viscosity values, which are considerably higher than those of water. The main difference is that here the velocity values are slightly lower in the developing profile when compared to NSFBF. The profiles for temperature differences of 10 °C and 50 °C are presented in Figures Figure 4.25 and Figure 4.26. Once again, these profiles are highly comparable to the NSFBF ones.

Lastly, the pressure results generated along the same line as those in the previous

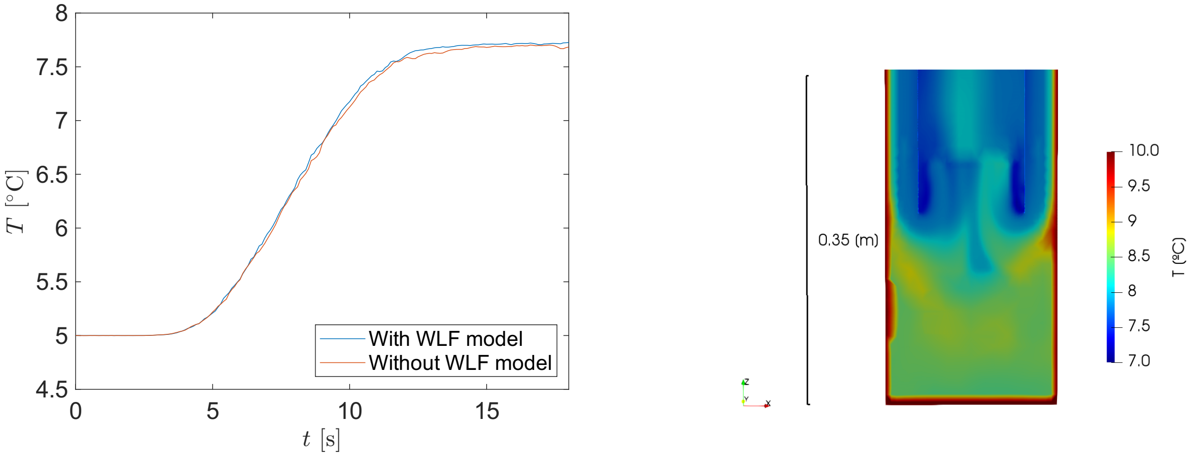

(a) Evolution of the average temperature at the outlet over time.

(b) Steady-state temperature contour in a frontal plane near the bottom of the well.

Figure 4.21: Results for the downhole heat exchanger process filled with a low-solid freshwater base fluid (LSFBF) subjected to a temperature difference of 5 °C.

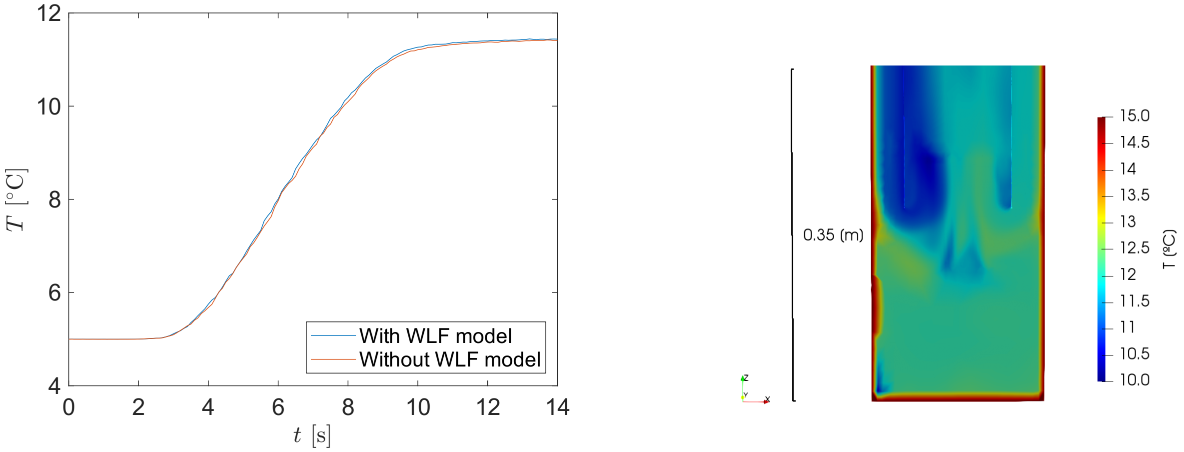

(a) Evolution of the average temperature at the outlet over time.

(b) Steady-state temperature contour in a frontal plane near the bottom of the well.

Figure 4.22: Results for the downhole heat exchanger process filled with a low-solid freshwater base fluid (LSFBF) subjected to a temperature difference of 10 °C.

sections are also shown in Figures 4.27, 4.28 and 4.29. Similarly to the previous fluids, the pressure p_{rgh} tends to increase with an increase in the temperature gradient. However, it is essential to note that this observation is specific to the instants for which the pressure was measured.

Figure 4.30 illustrates the comparison of the evolution of the pressure at the bottom of the DHE over time for the three temperature differences studied. Pressure values exhibit considerable fluctuation with an asymptotic behavior. Figure 4.30 also demonstrates that pressure values tend to generally increase with increasing temperature gradient.

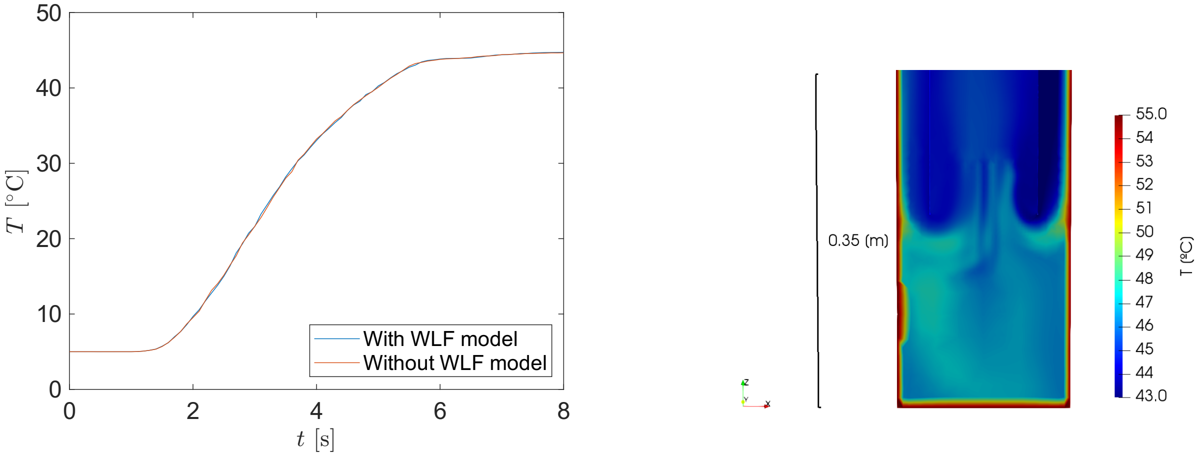

(a) Evolution of the average temperature at the outlet over time.

(b) Steady-state temperature contour in a frontal plane near the bottom of the well.

Figure 4.23: Results for the downhole heat exchanger process filled with a low-solid freshwater base fluid (LSFBF) subjected to a temperature difference of 50 °C.

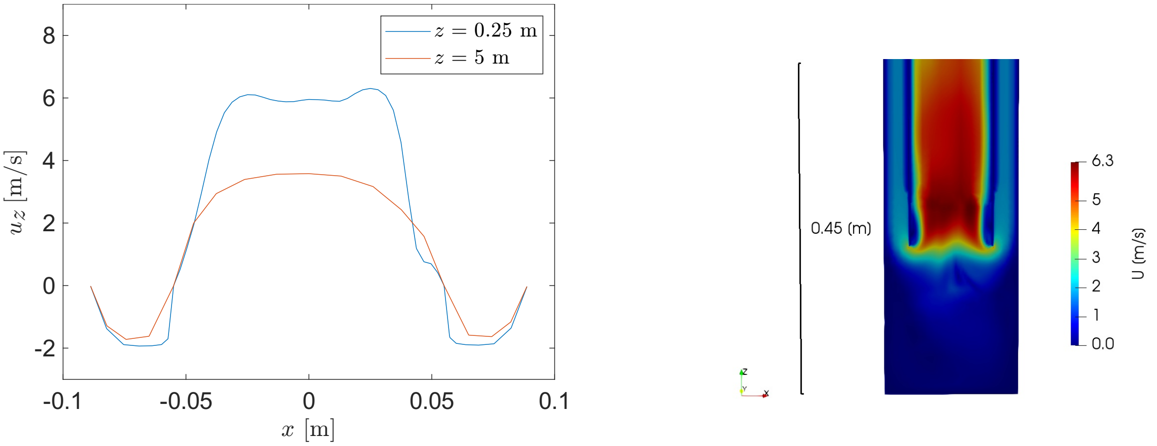

(a) Steady-state velocity profiles at two different heights.

(b) Steady-state velocity contour in a frontal plane near the bottom of the well.

Figure 4.24: Results for the velocity in the downhole heat exchanger process filled with a low-solid freshwater base fluid (LSFBF) subjected to a temperature difference of 5 °C.

4.4 Comparison of the different fluid results

To assess and compare the performance of the fluids used in this work, specifically water, NSFBF, and LSFBF the average temperature at the outlet of the well in steady-state will be compared. The results of this comparison are illustrated in Figures 4.31 and 4.32. The behaviors of the two polymer-based fluids were quite similar, with NSFBF exhibiting superior performance, except for a temperature difference of 50 °C, where they performed similarly. This is likely attributed to the more pronounced thermo-thickening effect in NSFBF. However, the water outperformed both fluids. These results suggest that for relatively simple systems such as the single DHE, where the fluid pathways are not highly intricate, the simplest fluid, water, remains the optimal choice in terms of achieving the highest temperature. However,

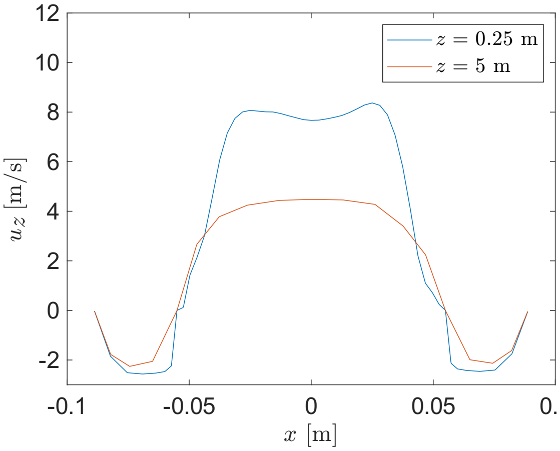

Figure 4.25: Steady-state velocity profiles at two different heights in the downhole heat exchanger process filled with a low-solid freshwater base fluid (LSFBF) subjected to a temperature difference of 10 °C.

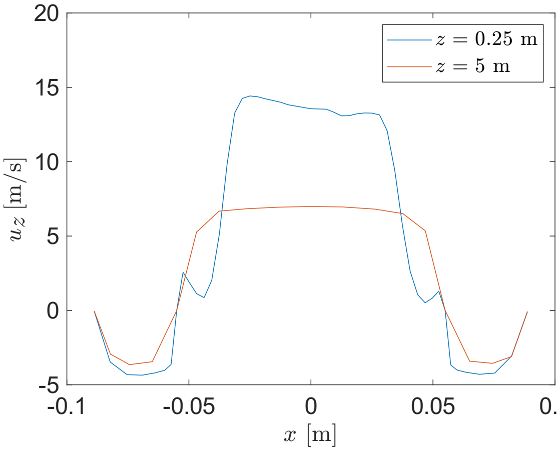

Figure 4.26: Steady-state velocity profiles at two different heights in the downhole heat exchanger process filled with a low-solid freshwater base fluid (LSFBF) subjected to a temperature difference of 50 °C.

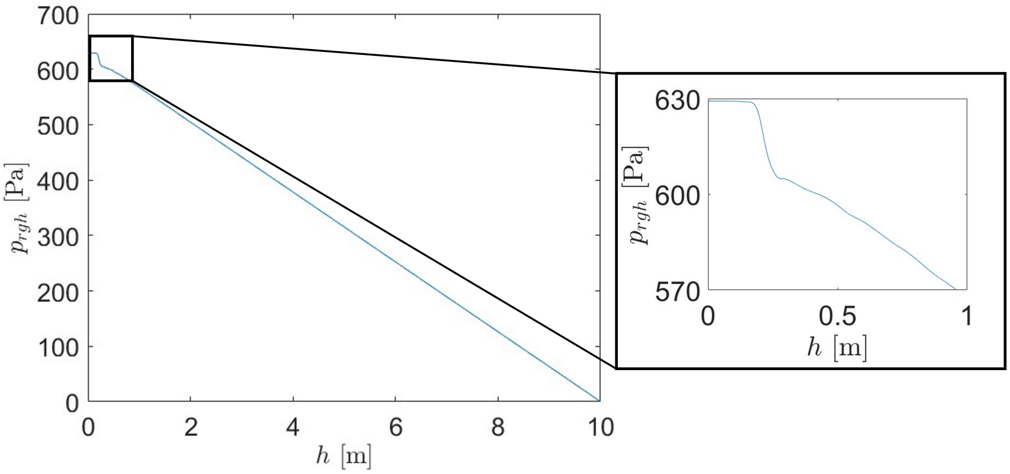

Figure 4.27: Pressure variation along the well height in the downhole heat exchanger process filled with a low-solid freshwater base fluid (LSFBF) subjected to a temperature difference of 5 °C, at time equal to 18 s.

for polymeric fluids, the findings indicate a significant benefit from the thermo-thickening effect, demonstrating its advantage in enhancing performance.

The discrepancy in viscosity among the three fluids plays a significant role in the obtained results, particularly when comparing the velocity profiles. This distinction is visually evident in Figure 4.33. For thermo-thickening fluids, viscosities were recorded at a temperature of 90 °C for this comparison. In Figure 4.34, the impact of viscosity on velocity is evident. Due to its lower viscosity, water attains higher velocities and achieves the maximum velocity over a larger portion of the cross-section compared to non-Newtonian fluids. This leads to a higher flow rate and, consequently, to a faster attainment of the steady-state.

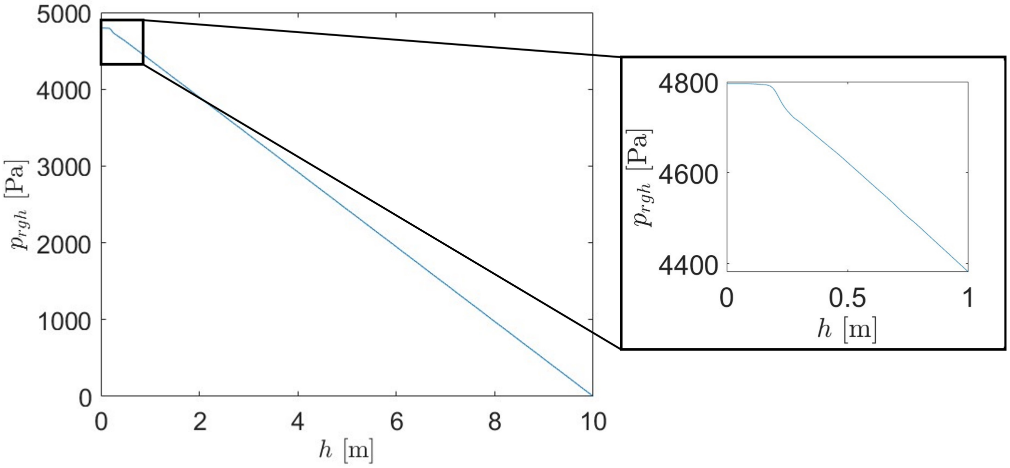

Figure 4.28: Pressure variation along the well height in the downhole heat exchanger process filled with a low-solid freshwater base fluid (LSFBF) subjected to a temperature difference of 10 °C, at time equal to 18 s.

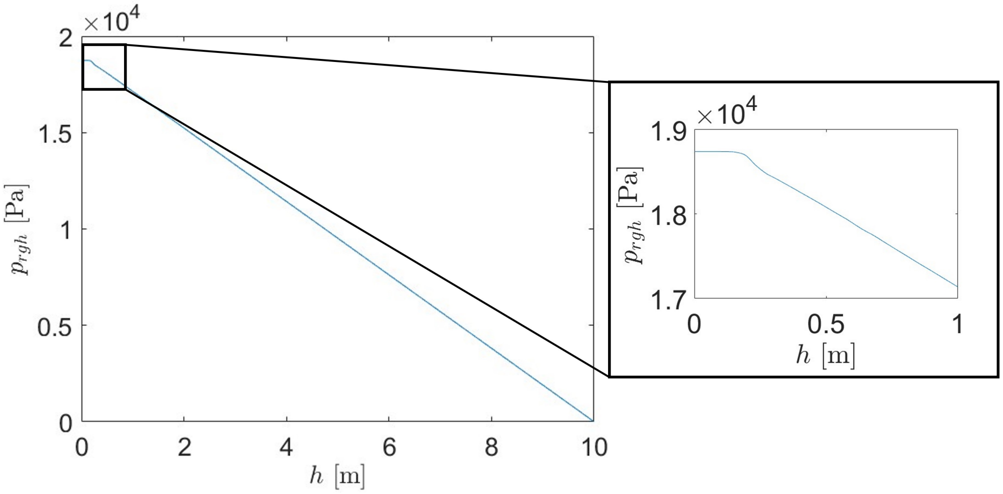

Figure 4.29: Pressure variation along the well height in the downhole heat exchanger process filled with a low-solid freshwater base fluid (LSFBF) subjected to a temperature difference of 50 °C, at time equal to 9 s.

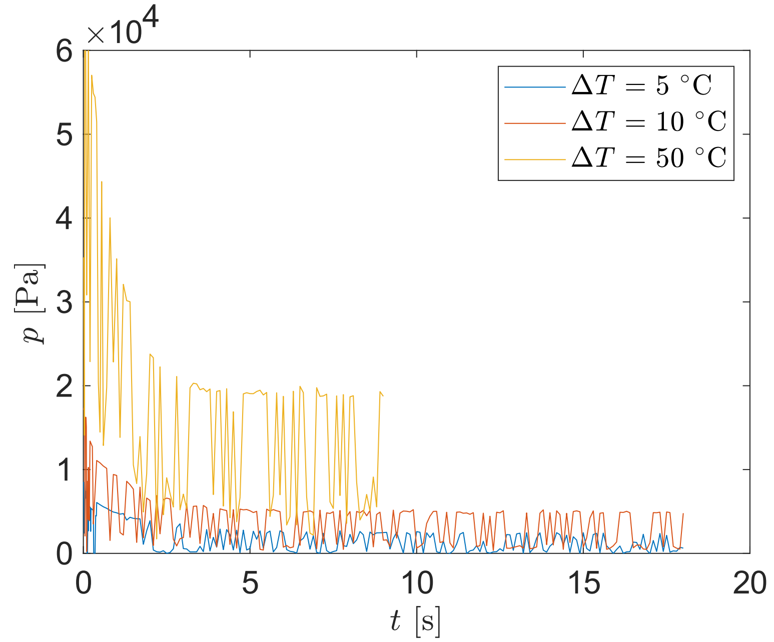

Figure 4.30: Evolution of the pressure at the bottom of the downhole heat exchanger over time for a low-solid freshwater base fluid (LSFBF) with different well temperature differences.

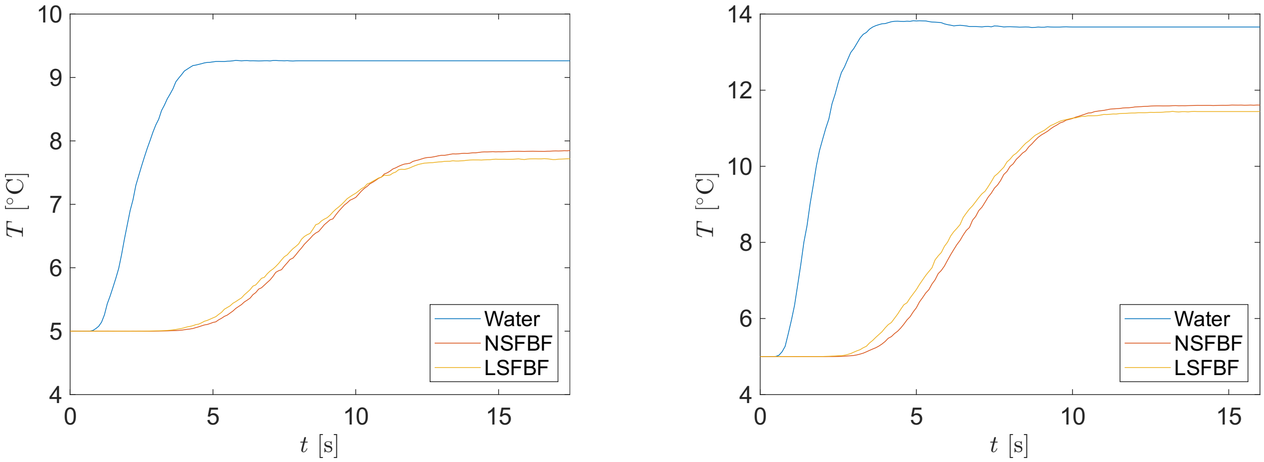

(a) Bottom well temperature of 10 °C.

(b) Bottom well temperature of 15 °C.

Figure 4.31: Comparison of the evolution of the temperature over time between all three fluids studied.

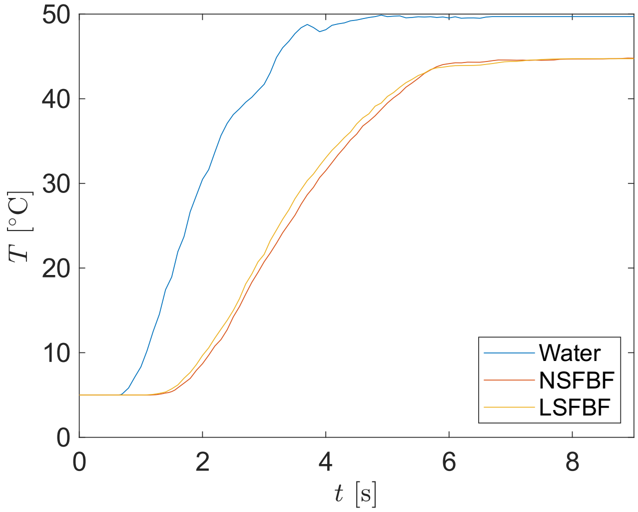

Figure 4.32: Comparison of the evolution of the temperature over time between all three fluids studied for a temperature difference of 50 °C.

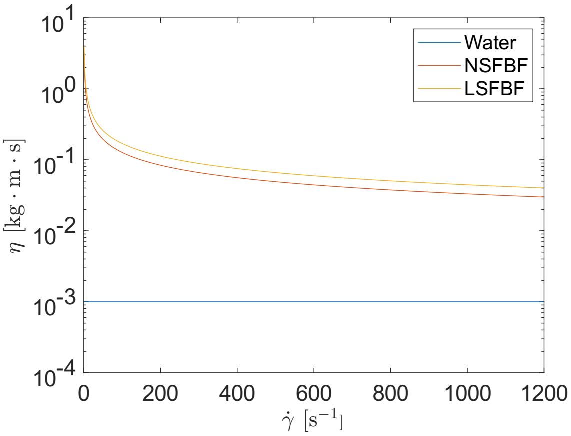

Figure 4.33: Comparison of the viscosity values versus shear-rate for the three fluids studied in this work.

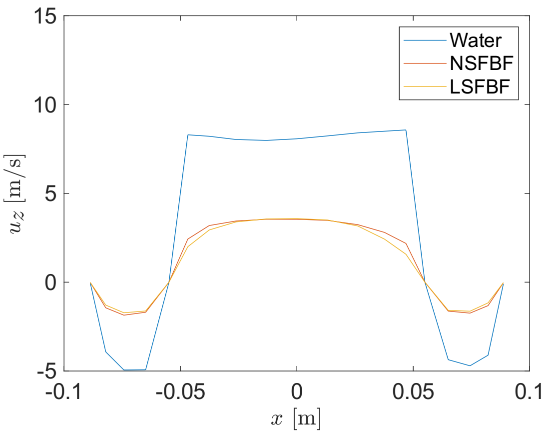

Figure 4.34: Comparison of the developed velocity profiles (taken at $z = 5$ m) for the three fluids.

Chapter 5

Conclusions and Future Work

In summary, the outcomes of the numerical simulations conducted for the Downhole Heat Exchanger (DHE) in enhanced geothermal systems (EGS) offer insights into the performance of thermo-responsive fluids compared to Newtonian fluids. The results reveal that the water consistently reached the highest temperatures, 9.3 °C, 13.7 °C, and 49.7 °C for thermal gradients of 5 °C, 10 °C, and 50 °C along the well, respectively. This is likely due to the simplicity of the geometry in the DHE. Due to the absence of intricate pathways for water to flow, the likelihood of a short circuit occurring was minimal.

Furthermore, the comparison between thermo-responsive fluids, such as the non-solid freshwater base fluid (NSFBF) and the low-solid freshwater base fluid (LSFBF), demonstrates the influence of the thermo-thickening effect on performance. Notably, NSFBF outperforms LSFBF, attributed to its higher thermo-thickening effect. The observed improvements in efficiency when using fluids with enhanced rheological characteristics highlight the potential for tailoring fluid properties to specific applications within the geothermal energy sector.

Some improvements that could improve efficiency involve refining the geometry. Smoothing the region where the fluid transitions from the descending region to the ascending region could be beneficial in reducing flow recirculation, allowing for a more uniform flow. Additionally, increasing the length of the inner wall to closer to the bottom of the well is another potential enhancement. In the case studied in this work, the gap was 0.2 m and could be reduced to a smaller value, such as 0.05 m, for example. Given the significant temperature reduction when moving slightly away from the bottom of the well and considering the low velocities in the region near it (as depicted in the temperature and velocity contour plots), having the fluid flow closer to the bottom could enhance heat transfer and increase efficiency.

Although water remains the preferred choice for the studied DHE geometry, the enhanced performance of the thermo-responsive fluid, especially NSFBF, indicates a promising avenue for further exploration and optimization. Future work could go into studying fluid flow for more complex geometries where short-circuiting is more likely to occur. In addition, applying a more complex rheological model for the fluid (in contrast to the Herschel-Bulkley model) could also give a more complete analyses of the flow.

Bibliography

[1] G. Bellini, K. Inoue, F. Mantovani, A. Serafini, V. Strati, and H. Watanabe. Geoneutrinos and geoscience: an intriguing joint-venture. *La Rivista del Nuovo Cimento*, pages 1–105, 2022.

[2] M. Estrada. Radiogenic Heat. `http://large.stanford.edu/courses/2014/ph241/estrada1/`, 2015.

[3] E. Barbier. Geothermal energy technology and current status: an overview. *Renewable and sustainable energy reviews*, 6:3–65, 2002.

[4] G. Kuo. Geothermal energy. *World Future Review*, 4:5–7, 2012.

[5] P. Olasolo, M. C. Juárez, M. P. Morales, S. D´Amico, and I. A. Liarte. Enhanced geothermal systems (EGS): A review. *Renewable and Sustainable Energy Reviews*, 56:133–144, 2016.

[6] D. Duchane and D. Brown. Hot dry rock (HDR) geothermal energy research and development at Fenton Hill, New Mexico. *Geo-Heat Centre Quarterly Bulletin*, 23, 2002.

[7] Bestec. The European Research Project. `https://www.bestec-for-nature.com/index.php/en/projects-en/soultz-en`, 2018.

[8] T. Koelbel and A. Genter. Enhanced geothermal systems: the Soultz-sous-Forêts project. In *Towards 100% Renewable Energy: Techniques, Costs and Regional Case-Studies*, pages 243–248. Springer, 2017.

[9] S.-M. Lu. A global review of enhanced geothermal system (EGS). *Renewable and Sustainable Energy Reviews*, 81:2902–2921, 2018.

[10] C. Zhong, T. Xu, F. Gherardi, and Y. Yuan. Comparison of CO_2 and water as working fluids for an enhanced geothermal system in the Gonghe Basin, northwest China. *Gondwana research*, 122:199–214, 2023.

[11] D. W. Brown. A hot dry rock geothermal energy concept utilizing supercritical CO_2 instead of water. In *Proceedings of the twenty-fifth workshop on geothermal reservoir engineering, Stanford University*, pages 233–238, 2000.

[12] B. Gee, R. Gracie, and M. B. Dusseault. Multiscale short-circuiting mechanisms in multiple fracture enhanced geothermal systems. *Geothermics*, 94:102094, 2021.

[13] M. Wei, Y. Gao, X. Li, and M. J. Serpe. Stimuli-responsive polymers and their applications. *Polymer Chemistry*, 8:127–143, 2017.

[14] K. Jain, R. Vedarajan, M. Watanabe, M. Ishikiriyama, and N. Matsumi. Tunable LCST behavior of poly (N-isopropylacrylamide/ionic liquid) copolymers. *Polymer Chemistry*, 6:6819–6825, 2015.

[15] N. A. Cortez-Lemus and A. Licea-Claverie. Poly (N-vinylcaprolactam), a comprehensive review on a thermoresponsive polymer becoming popular. *Progress in Polymer Science*, 53:1–51, 2016.

[16] L. D. W. Djouonkep, B. Xie, H. Tao, L. Zhuo, A. P. Tchameni, and L. Zhao. Investigating the structure-to-property of thermo-thickening polymers capped by different structural side chains. *Reactive and Functional Polymers*, 186:105569, 2023.

[17] S. M. Åsen, A. Stavland, and D. Strand. Flow behavior of thermo-thickening associative polymers in porous media: effects of associative content, salinity, time, velocity, and temperature. *SN Applied Sciences*, 4, 2022.

[18] B. Xie, X. Liu, H. Wang, and L. Zheng. Synthesis and application of sodium 2-acrylamido-2-methylpropane sulphonate/N-vinylcaprolactam/divinyl benzene as a high-performance viscosifier in water-based drilling fluid. *Journal of Applied Polymer Science*, 133, 2016.

[19] B. Xie, Z. Qiu, W. Huang, J. Cao, and H. Zhong. Characterization and Aqueous Solution Behavior of Novel Thermo-associating Polymers. *Journal of Macromolecular Science, Part A*, 50:230–237, 2013.

[20] B. Xie and X. Liu. Thermo-thickening behavior of LCST-based copolymer viscosifier for water-based drilling fluids. *Journal of Petroleum Science and Engineering*, 154:244–251, 2017.

[21] Y. Shangguan, M. Liu, L. Jin, M. Wang, Z. Wang, Q. Wu, and Q. Zheng. Thermo-thickening behavior and its mechanism in a chitosan-graft-polyacrylamide aqueous solution. *Soft Matter*, 14:6667–6677, 2018.

[22] X. Chen, C. Wang, Y. Wang, H. Wang, and R. Wang. Prevention Strategy of Cement Slurry Sedimentation under High Temperature. Part 1: A Polymer with Continuous Thermo-Thickening Behavior from 48 to 148 °C. *The Journal of Physical Chemistry C*, 123:18573–18584, 2019.

[23] R. P. Chhabra and J. F. Richardson. *Non-Newtonian flow and applied rheology: engineering applications*. Butterworth-Heinemann, 2011.

[24] W. H. Herschel. Measurement of consistency of rubber-benzene solutions. *Kolloid-zeitschrift*, 39:291–298, 1926.

[25] M. L. Williams, R. F. Landel, and J. D. Ferry. The Temperature Dependence of Relaxation Mechanisms in Amorphous Polymers and Other Glass-forming Liquids. *Journal of the American Chemical society*, 77:3701–3707, 1955.

[26] F. Pimenta and M.A. Alves. rheoTool. `https://github.com/fppimenta/rheoTool`. Accessed: August 2023.

[27] F.A. Morrison. *Understanding Rheology*. Raymond F. Boyer Library Collection. Oxford University Press, 2001.

[28] Autodesk CFD. Finite Element vs Finite Volume. `https://help.autodesk.com/view/SCDSE/2024/ENU/?guid=GUID-12A9AED8-2047-4D3A-BC80-82BE9CF47517`, 2024.

[29] F. Moukalled, L. Mangani, and M. Darwish. *The Finite Volume Method*. Springer, 2016.

[30] W. Huang, W. Cao, and F. Jiang. A novel single-well geothermal system for hot dry rock geothermal energy exploitation. *Energy*, 162:630–644, 2018.

[31] X. Bu, Y. Ran, and D. Zhang. Experimental and simulation studies of geothermal single well for building heating. *Renewable Energy*, 143:1902–1909, 2019.

[32] FreeCAD. FreeCAD Documentation. `https://wiki.freecad.org/Main_Page`, 2023.

[33] C. Greenshields and H. Weller. *Notes on Computational Fluid Dynamics: General Principles*. CFD Direct Ltd, Reading, UK, 2022.

[34] C. Greenshields. *OpenFOAM v11 User Guide*. The OpenFOAM Foundation, London, UK, 2023.

[35] Andrew L Gerhart, John I Hochstein, and Philip M Gerhart. *Munson, Young and Okiishi's Fundamentals of Fluid Mechanics*. John Wiley & Sons, 2020.